Effects of Nonlinear Soil Behavior on Kappa (κ): Observations from the KiK-Net Database

Chunyang Ji, Ashly Cabas, Luis Fabian Bonilla, Céline Gelis

Effects of Nonlinear Soil Behavior on Kappa (κ): Observations from the KiK-Net Database

Article *in* Bulletin of the Seismological Society of America · April 2021

DOI: 10.1785/0120200286

4 authors:

Chunyang Ji
North Carolina State University
8 PUBLICATIONS **38** CITATIONS
SEE PROFILE

Ashly Cabas
North Carolina State University
37 PUBLICATIONS **171** CITATIONS
SEE PROFILE

Luis Fabian Bonilla
Université Gustave Eiffel
140 PUBLICATIONS **3,693** CITATIONS
SEE PROFILE

Celine Gelis
Institut de Radioprotection et de Sûreté Nucléaire (IRSN)
89 PUBLICATIONS **1,409** CITATIONS
SEE PROFILE

Effects of Nonlinear Soil Behavior on Kappa (κ): Observations from the KiK-net database

Ji, Chunyang, Cabas, Ashly, Bonilla, Luis Fabian, and Gelis, Céline

Declaration of competing interests

The authors acknowledge there are no conflicts of interest recorded.

Abstract

Soil nonlinear behavior is often triggered in soft sedimentary deposits subjected to strong ground shaking and has led to catastrophic damage to civil infrastructure in many past earthquakes. Nonlinear behavior in soils is associated with large shear strains, increased material damping ratio and reduced stiffness. However, most investigations of the high-frequency spectral decay parameter κ, which captures attenuation, have focused on low-intensity ground motions inducing only small shear strains. Because studies of the applicability of the κ-model when larger deformations are induced are limited, this paper investigates the behavior of κ (both κ_r per record and site-specific κ_0 estimates) beyond the linear-elastic regime. Twenty stations from the KiK-net database, with time-average shear wave velocities in the upper 30 m between 213 and 626 m/s, are used in this study. We find that the classification scheme used to identify ground motions that trigger soil nonlinear behavior biases estimates of κ_0 in the linear and nonlinear regimes. A hybrid method to overcome such bias is proposed considering proxies for in situ deformation (via the shear strain index) and ground shaking intensity (via peak ground acceleration). Our findings show that soil nonlinearity affects κ_r and κ_0 estimates, but this influence is station-dependent. Most κ_0 at our sites had a 5-20% increase at the onset of soil nonlinear behavior. Velocity gradients and impedance contrasts influence the degree of soil nonlinearity and its effects on κ_r and κ_0. Moreover, we observe that other complexities in the wave propagation phenomenon (e.g., scattering and amplifications in the high-frequency range) impose challenges to the application of the κ_0-model, including the estimation of negative values of κ_r.

Introduction

The anelastic attenuation of seismic waves as they travel through sedimentary deposits is a function of the deformations induced, which in turn depend on the material properties (e.g., plasticity of the soil) and the intensity of the ground shaking. Material damping ratio, ξ, is commonly used in geotechnical earthquake engineering to quantify viscous and anelastic energy dissipation in soils subjected to dynamic loading. Empirical models of ξ often have a constant minimum value (known as the minimum shear-strain damping, ξ_{min}) for small shear strains considered in the linear-elastic regime (e.g., Darendeli, 2001). Yet, values of ξ increase as larger shear strains are induced in soil deposits by stronger ground excitations (Idriss et al. 1978, Seed et al. 1986, Darendeli 2001). The characterization of ξ across a wide range of strains is essential to model the effects of local soil conditions on earthquake ground motions.

The high-frequency spectral decay parameter κ was introduced by Anderson and Hough (1984) based on the Fourier spectrum characteristics of a ground motion's shear-wave window recorded directly in the field, which makes it an observable parameter that quantifies total attenuation (e.g., energy dissipation caused by scattering and anelasticity). Estimates of κ have proven useful in multiple applications, from stochastic modeling of ground motions (Boore 2003) to the development of host-to-target adjustments of ground motion models (e.g., Campbell 2003, Al Atik et al. 2014). The site-specific, distance-independent component of κ, known as κ_0 (Anderson 1991), is defined as a site parameter that captures the attenuation due to the propagation of seismic waves through near-surface materials. The relationship between κ_0 and ξ_{min} has been investigated in previous studies (e.g., Cabas et al. 2017; Ktenidou et al. 2015; Xu et al. 2019) for weak motion data, but the quantification of κ and κ_0 beyond the linear-elastic regime remains unsolved.

Most studies on individual estimates of κ (i.e., the value measured from the observed Fourier Amplitude Spectra (FAS) per record following the Anderson and Hough (1984) approach), hereafter referred to as κ_r, and its site-specific component κ_0 have used ground motion records that do not trigger nonlinear behavior at the sites of interest or that are not considered influenced by the site's nonlinear response (e.g., Ktenidou et al. 2013, Van Houtte et al. 2011, Laurendeau et al. 2013, Edwards et al. 2015, Perron et al. 2017, Xu et al. 2019). However, nonlinear soil behavior has often been responsible for increasing the damage potential of strong ground motions in past earthquakes (e.g., Darragh and Shakal, 1991, Trifunac and Todorovska, 1994, Bonilla et al., 2011, Rong et al., 2016). Understanding near-surface attenuation effects in the nonlinear regime is then necessary for a thorough assessment of seismic hazards and risks imposed to civil infrastructure (Anderson and Hough 1984). Hence, this paper investigates the relationships among κ, shear strains and ground motion intensity to understand the behavior of κ at the onset of nonlinear soil behavior.

Background

The first paper that attempted to connect soils' nonlinear response and κ_r was conducted by Yu et al. (1992), where the authors compared two simulated records: one from a linear site response analysis, and the other from a time-domain nonlinear site response analysis. Yu et al. (1992) observed that the value of κ_r estimated with the Anderson and Hough (1984) approach and corresponding to the motion affected by soil nonlinearity was smaller. However, later studies found a positive correlation between κ_r (and κ_0), strain amplitudes and the intensity of ground shaking (e.g., Durward et al 1996; Lacave-Lachet et al 2000; Dimitriu et al. 2001).

Durward et al. (1996) found that κ_r values were a function of peak ground velocity (PGV, varying from 0.01 to 1 m/s), which was used as a proxy for deformation. Values of κ_r were computed for more than 60 records observed at 23 sites in the Imperial Valley, California based on the acceleration spectrum approach (Anderson and Hough, 1984). Durward et al. (1996) hypothesized that soil nonlinearity had affected κ_r because higher κ_r values correlated well with higher PGVs. Moreover, Lacave-Lachet et al. (2000) analyzed ground motions from the 1995 Kobe earthquake in Japan (i.e., the main shock and aftershocks), and found that κ_r values increased with increasing peak ground acceleration (PGA). Hence, Lacave-Lachet et al. (2000) proposed to use κ_r to detect the onset of soil nonlinearity. Dimitriu et al. (2001) investigated the dependency between site-specific κ_0 and ground shaking intensity. Values of κ_r for 23 ground motions (i.e., 46 horizontal components with values of κ_r reported for each individual component) were computed at two adjacent sites in Lefkas, western Greece, based on the acceleration spectrum method. Dimitriu et al. (2001) provided evidence that κ_0 was a proxy for soil nonlinearity based on the observed dependency between κ_0 and ground shaking amplitudes, which were represented by mean horizontal acceleration in the S-wave window (MGA), PGA, and PGV. Positive correlations were found between the 46 κ_0 values and MGA, PGA, and PGV in log-scale, while a negative correlation was observed between κ_0 and the site dominant-resonance frequency. However, Van Houtte et al. (2014) identified an opposite correlation between estimates of κ_0 (computed as the individual measured κ_r with epicentral distance less than 30 m) and PGA at hard sites (i.e., with V_{s30} varying from 422 to 1073 m/s) using ground motions from the 2010-2011 Canterbury earthquake sequence in New Zealand. The authors suggested further investigations to understand the associated physical mechanism.

There are still few and contradicting observations of the effects of nonlinearity on κ_r and κ_0 estimates (Ktenidou et al. 2015). Previous studies only considered a very limited database of ground motions. This paper takes advantage of the unique Japanese Kiban-Kyoshin network (KiK-net), which is rich in high-quality ground motions, to further investigate the effects of soil nonlinearity on κ_r and κ_0. More specifically, we explore the dependence of κ_r and κ_0 on ground shaking intensity (i.e., weak, moderate or strong ground motions as parameterized by PGA), and on the level of shear strains induced in near-surface materials at 20 KiK-net stations. First, we present the conceptual basis for the relationship between κ, shear strains and ground motion intensity. Then, we describe our database and methods, starting with the identification of an appropriate classification scheme for linear and nonlinear ground motions. The analysis of the effects of ground shaking amplitudes on κ_r at each study site follows. Lastly, we compare the ratio of nonlinear and linear site-specific κ_0 across all selected stations to assess the variation of near-surface attenuation estimates from the linear-elastic to the nonlinear regime.

Conceptual basis for the interpretation of κ beyond the linear-elastic regime

The induced strain level in a given soil layer is a function of the material properties, and the amplitude and frequency content of the incoming wavefield at the site. Stronger ground shaking results in larger-strain responses, which produce an increase in material damping ratio (in combination with a reduction of shear modulus). The short wavelength of high frequency waves allows for multiple cycles of shearing in near-surface sedimentary layers, which makes them more sensitive to the effects of a higher material damping ratio. Thus, we hypothesize that stronger

ground shaking inducing larger deformations in sedimentary deposits will affect estimates of the high-frequency spectral decay parameter κ.

Figure 1 serves as an example to illustrate this hypothesis. The acceleration FAS and empirical transfer function (ETF) corresponding to a pair of ground motions recorded at depth and at the ground surface at FKSH14 are shown. FKSH14 is one of the 20 KiK-net station analyzed in this work (see Database description). One of the ground motion pairs has a low ground shaking intensity (with a surface PGA of less than 0.1 m/s^2 for both horizontal components), while the other one has a higher ground shaking intensity (with a surface PGA of 0.71 m/s^2 and 0.25 m/s^2 for the H_1 and H_2 components, respectively). Values of κ_r per record are also estimated for both pairs. To minimize the bias from path effects and isolate local site effects on κ_r values per record, the selected weak and strong ground motions in Figure 1 correspond to events with similar focal depths, azimuths and epicentral distances (i.e., the focal depths, azimuths and epicentral distances are 5 km, 319^o, and 15.04 km, respectively for the low-intensity event, and 5 km, 323^o, and 15.79 km, respectively for the high-intensity event). The moment magnitudes of the events associated with the weak and strong ground motions in Figure 1 are 4.0 and 5.1, respectively. To reduce the variability associated with the calculation of κ_r from the acceleration spectrum method, we use the same frequency window for all ground motions (Edwards et al. 2011).

Larger values of κ_r at the ground surface (e.g., 0.071 s for the horizontal component H_1) are obtained for the high-intensity ground motion compared to the corresponding κ_r values for the low-intensity ground motion (e.g., 0.057 s for H_1). Likewise, the high-intensity ground motion results in a larger κ_{TF} (Drouet et al. 2010), which is computed on the decaying portion of the

157 empirical transfer function at high frequencies and is equivalent to $\Delta\kappa$ (i.e., $\kappa_{r\_sur} - \kappa_{r\_bor}$) estimates
158 when using the same frequency band for calculation purposes. The value of κ_{TF} corresponding to
159 the high-intensity and low-intensity motions are 0.026 s and 0.019 s, respectively. Meanwhile, the
160 ETF corresponding to the high-intensity event shows lower amplifications at higher frequencies
161 (e.g., amplification ranges from 1 to 2 between 15 and 30 Hz for H_1 approximately) than its
162 counterpart for the low-intensity ground motion (i.e., amplification ranges from 2 to 3 between 15
163 and 30 Hz for H_1 approximately), which reflects the stronger influence of increased material
164 damping ratio on high frequencies.
165
166 Values of κ_r and $\Delta\kappa$ (or κ_{TF} in Figure 1) are identical for the high- and low-intensity records for
167 the H_2 component. It must be noted that the difference in PGA between the low- and high- intensity
168 surface ground motions is less significant for the H_2 components than that for the H_1 components,
169 while the PGAs at depth are very similar (i.e., the borehole PGAs for the high-intensity motion are
170 0.06 and 0.07 m/s^2 for H_1 and H_2 components, respectively; the borehole PGAs for the low-
171 intensity motion are 0.01 m/s^2 for both H_1 and H_2 components). This may explain why $\Delta\kappa$ values
172 are the same for the low and high intensity motions in the H_2 component direction. Additionally,
173 this observation also hints that the near-surface attenuation and site effects may be affected by the
174 ground motion directionality as shown by Ji et al. (2020). Finally, soil nonlinearity is commonly
175 observed at shallower layers (Régnier et al. 2013), and their effects on κ_r at borehole are smaller
176 than at surface. Thus, the κ_r at borehole should be less affected by soil nonlinearity because it
177 nonlinear soil behavior is less likely to be triggered at depth (e.g., the borehole V_s at FKSH14 is
178 1210 m/s with borehole sensor depth of 147 m). In Figure 1, values of κ_r at borehole are similar
179 for the high- and low-intensity motions. The changes in κ_r shown in Figure 1 exemplify the need

to further investigate the influence of the onset of soil nonlinearity on κ_r as well as the potential implications on κ_0 values at a specific site.

Database description

In this study, we use ground motions from the KiK-net database, which provides high quality strong ground motions recorded at more than 600 stations installed uniformly across Japan. Each station possesses a pair of sensors, one at the surface and another one at depth that is typically between 100 to 200 m deep. The sampling frequency of the observed acceleration series is either 100 or 200 Hz. The P- and S-wave velocity profiles are measured by downhole PS logging and available at the KiK-net website (see Resources and Data). The earthquake information, including the seismic moment magnitude M_w, focal depth and epicenter location are provided by the broadband seismography network (F-net) catalog. The dataset used in this work was processed by Bahrampouri et al. (2020) with an automated protocol, which corrects the baseline and removes the background noise with a bandpass/high-pass acausal filter. The low-frequency filter corner frequency is determined based on a required value of the (signal+noise)/noise equal to 3, corresponding to a signal-to-noise ratio (SNR) of 2.0 (Boore and Bommer, 2005); this frequency ranges between predetermined minimum and maximum values of 0.05 and 0.5 Hz, respectively. The minimum high-frequency filter corner frequency is determined for a SNR of 1.0 (Douglas and Boore 2011). The minimum bandpass width is 60% of the range defined from zero to the Nyquist frequency. Further detailed descriptions on the ground motion processing are available in Bahrampouri et al. (2020).

We use surface and borehole records (only horizontal components) in this paper. The criteria applied to select records are as follows: (1) epicentral distance is less than 150 km, (2) the SNR ratio is larger than 3.0 at each frequency from 1.0 to 30 Hz, (3) focal depth is less than 35 km (Ji et al. 2020), and (4) the seismic wave path does not cross the Japanese volcanic belt (Nakano et al. 2015). Thus, twenty stations with more than five nonlinear ground motions (the definition of nonlinear ground motions is described next in the Methods section) are used in this work (with 18 stations having more than 10 nonlinear records and 8 stations having more than 15 nonlinear records, see Table 1). Table 1 provides local soil conditions and the number of ground motions at each selected site. The locations of selected stations are shown in Figure 2a, while the magnitude and distance distribution of selected ground motions is provided in Figure 2b.

Method

Identification of the onset of nonlinearity

Identifying ground motions that trigger soil nonlinear behavior is key to evaluate κ estimates beyond the linear-elastic regime empirically. The shear-strain index ($I_\gamma = PGV/V_s$), which is a proxy for the in-situ deformation, and PGA, which describes the peak amplitude of the ground motion, are commonly used to differentiate linear from nonlinear ground motions (e.g., Xu et al. 2019, Cabas et al. 2017, Wang et al. 2019). Moreover, the correlation between PGA and I_γ has been shown to be an effective proxy to capture in-situ stress-strain relationships. This correlation has been characterized via the classic hyperbolic model, which fits empirical observations (Chandra et al. 2014, 2015, Guéguen et al. 2018). However, there is lack of consensus regarding the sufficiency and efficiency of existing proxies associated with the onset of nonlinear behavior. For example, Xu et al. (2019) assumed that records with I_γ less than 0.01% are linear ground

225 motions, while Cabas et al. (2017) adopted 0.1%. On the other hand, Ktenidou et al. (2013) chose
226 a PGA of 0.1 m/s^2 as the threshold for linear ground motions. Régnier et al. (2013) conducted a
227 statistical analysis on the KiK-net dataset to understand nonlinear site response at their stations.
228 They characterized linear soil behavior as that associated with motions with a PGA at depth less
229 than 0.1 m/s^2.
230
231 We develop appropriate criteria to identify nonlinear ground motions based on PGA and I_γ. In this
232 paper, the shear-strain index at the surface ($I_{\gamma,0}$) is defined as follows:

233 $$I_{\gamma,0} = PGV_{rotD50} / V_{s,0} \quad (1)$$

234 where $V_{s,0}$ is the shear-wave velocity at the ground surface, and PGV_{rotD50} is the median PGV for
235 all rotated surface ground motions following the approach of Boore (2010). The use of PGV_{rotD50}
236 rather than the PGV from recorded ground motion horizontal components can minimize
237 directionality effects. The use of $I_{\gamma,0}$ (Equation 1) as an indicator of the onset of soil nonlinearity
238 has some limitations though. First, the selection of single V_s and PGV values to capture the depth-
239 dependent deformation in the profile may underestimate or overestimate the level of nonlinearity
240 experienced across the whole column. Thus, $I_{\gamma,0}$, as defined in Equation 1, serves simply as a proxy
241 for a representative shear strain to take place in the sedimentary deposit of interest. Notably, there
242 is no consensus regarding the most appropriate choice of V_s for I_γ estimates. For example, V_{s30} is
243 a commonly used site proxy and hence often selected to compute I_γ (e.g., Kim et al. 2016, Guéguen
244 et al. 2018). The equivalent V_s measured between two successive sensors with seismic
245 interferometry by deconvolution has also been adopted for I_γ estimates (e.g., Chandra et al. 2015,
246 2016, Wang et al. 2019). Second, values of $I_{\gamma,0}$ are not directly comparable to shear strains
247 measured in the laboratory, not only because I_γ is a proxy and not a measured value, but also

because the dissipation of seismic energy as captured in the laboratory may not fully represent the attenuation mechanisms taking place in the field (Cabas et al. 2017).

By applying the classic hyperbolic model to describe the correlation between PGA_{rotD50} and $I_{\gamma,0}$, we find that there is no unique threshold to identify nonlinear ground motions across all study sites. Figure 3 provides examples of theoretical hyperbolic fitting curves at four stations (i.e., IBRH16, IBRH17, IBRH20 and IWTH21) with varying V_{s30} values (from 244 to 626 m/s) to demonstrate the limitations associated with using a single parameter to identify nonlinear ground motions at multiple sites. Scatter points represent PGA_{rotD50} and $I_{\gamma,0}$ pairs from recorded ground motions at the sites of interest, while the lines correspond to the fitting curves from the hyperbolic model. It is observed that the same deformation at various sites would be triggered by different levels of ground shaking (e.g., $I_{\gamma,0}$ of 0.05% will be caused by a PGA_{rotD50} around 1 m/s^2 at a NEHRP D site, such as IBRH20 with V_{s30} of 244 m/s, and by a PGA_{rotD50} of 2 m/s^2 at a NEHRP C site, such as IBRH16 with V_{s30} of 626 m/s). On the other hand, if nonlinearity is assumed to be triggered when the PGA_{rotD50} is larger than a predetermined threshold, different levels of $I_{\gamma,0}$ will be associated with the onset of soil nonlinearity. Hence, in this work, we propose a hybrid method (further described in the next section) based on both, the intensity of the excitation and in-situ deformation to classify ground motions.

Linear, transitional, and nonlinear datasets

Surface and borehole ground motions are considered separately herein. Régnier et al. (2013) considered that records with borehole PGA less than 0.1 m/s^2 cannot trigger nonlinear site response at the ground surface. They also observed that soil nonlinearity is mainly triggered at superficial

layers. In this study, there are only 3% records with borehole PGA larger than 0.1 m/s^2. Therefore the borehole records are assumed to remain in the linear-elastic regime (i.e., they do not trigger nonlinear behavior at depth). Surface records are separated into three sub-datasets, namely linear, transitional (i.e., soil's behavior is between the linear-elastic and nonlinear regimes), and nonlinear ground motions. First, we define a threshold based on $I_{\gamma,0}$ to differentiate linear from transitional records, which is hereafter referred to as $I_{\gamma,0,l}$. Likewise, a transitional threshold, $I_{\gamma,0,t}$, is defined to separate transitional and nonlinear ground motions. The linear $I_{\gamma,0,l}$ threshold is defined as the onset of soil nonlinearity by visual inspections of the corresponding PGA_{rotD50} versus $I_{\gamma,0}$ curve, and corresponds to the point where PGA_{rotD50} values begin to increase at a higher rate with increasing $I_{\gamma,0}$. The transitional $I_{\gamma,0,t}$ threshold captures when the soil nonlinearity becomes more apparent, which corresponds to the point where the second change in slope of the PGA_{rotD50} versus $I_{\gamma,0}$ curve takes place. Figure 4 provides an example of the selection of $I_{\gamma,0,t}$ and $I_{\gamma,0,l}$ at station MYGH10. The threshold separating the linear and transitional ground motions is $I_{\gamma,0,l}$ = 0.001%, while the threshold separating transitional and nonlinear ground motions is $I_{\gamma,0,t}$ = 0.007%.

A maximum PGA_{rotD50} of 0.25 m/s^2, which is the value adopted by Régnier et al. (2016) to define low-amplitude motions, is chosen as an additional constraint to avoid linear ground motions being erroneously included into the nonlinear dataset. Thus, linear, transitional, and nonlinear datasets are defined as follows:

- Linear ground motions: records with $I_{\gamma,0}$ less than the $I_{\gamma,0,l}$ threshold.
- Nonlinear ground motions: records with (a) $I_{\gamma,0}$ larger than the $I_{\gamma,0,t}$ threshold and (b) PGA_{rotD50} larger than 0.25 m/s^2.
- Transitional ground motions: records not classified as either linear or nonlinear.

The validity of the proposed linear, transitional, and nonlinear datasets is tested by examining the behavior of the shear modulus, G against $I_{\gamma,0}$ at the study sites. The reduction of G for empirical ground motions is estimated as follows (after Guéguen et al., 2019):

$$G/G_{\max} = \frac{PGA_{rotD50}}{PGV_{rotD50}/V_{s,0}} \Bigg/ \left(\frac{PGA_{rotD50}}{PGV_{rotD50}/V_{s,0}} \right)_{\max} \quad (2)$$

The term $\left(\frac{PGA_{rotD50}}{PGV_{rotD50}/V_{s,0}} \right)_{\max}$ is computed from the corresponding average ratio of records with $I_{\gamma,0}$ less than 0.001%, which is the predetermined threshold of $I_{\gamma,0,l}$ for the linear-elastic deformation limit in this work. Figure 5 shows the G/G_{max} versus $I_{\gamma,0}$ curves at all study sites. Even though Figure 5 does not directly correspond to laboratory-based curves, it serves as a first order verification of the distinct behavior corresponding to the linear, transitional, and nonlinear ground motions identified with the categorization scheme proposed herein. One challenge when interpreting these data is the characterization of the soil volume being sampled when using I_{γ}, which is related to the frequency band that PGV is acting on. Identified linear ground motions mainly have G/G_{max} values around 1 (G/G_{max} values higher than 1 result from using mean G values as a proxy for G_{max}), while the ratios corresponding to the nonlinear dataset are generally less than 1 due to the onset of soil nonlinearity. Notably, values of G/G_{max} associated with the transitional dataset are between the linear and nonlinear datasets. It is not clear whether the site response associated with records identified as transitional could be equivalent to a linear-elastic or a nonlinear response, because associated G/G_{max} values vary within a single station and across stations. Hence, the characterization as transitional is deemed appropriate herein.

κ_{r_AS} estimates

We use the acceleration spectrum approach (Anderson and Hough, 1984) to estimate κ_{r_AS}. To minimize the variability introduced by the selection of the S-wave window, the entire time series is used. Because compatibility with engineering analysis such as geotechnical site response analysis and ground motion models is also desired, and such applications use complete time series, calculating κ_{r_AS} using the entire time series is convenient. Moreover, the differences of κ_{r_AS} values measured from S-wave window and the entire time series are not significant in most cases (Ji et al. 2020). In this study, a subset of randomly selected ground motions is used to further assess potential discrepancies between using the S-wave window relative to the entire time series, and no significant differences are observed. Hence, the entire time histories are used.

The variability in estimates of κ_{r_AS} is a function of the selection of the frequency band (Edwards et al. 2015, Perron et al. 2017) among other factors (Ji et al. 2020, Ktenidou et al. 2013). Moreover, soil nonlinearity affects low and high frequencies differently. The onset of nonlinear soil behavior can influence high frequencies first (Bonilla et al. 2011, Bonilla and Ben-Zion, 2020) because larger shear strains are induced in softer, thinner layers located at shallower depths (i.e., in a profile with increasing stiffness with depth). Hence, we compute κ_{r_AS} based on a pre-determined fixed frequency window ($[f_1, f_2]$). The pre-determined f_1 corresponds to the maximum value between 1.4 f_c (where f_c is the earthquake source corner frequency of each record) and 1.4 f_0 (where f_0 is the site's predominant frequency). Indeed, if f_1 is lower than f_0, the value of κ_{r_AS} will be biased by the site amplification in the high-frequency range (Parolai and Bindi 2004). On the other hand, the f_c requirement is added to reduce the effects of the earthquake source. The value of f_2 is set to be 25

337 Hz due to consideration of KiK-net instrument's response (Aoi et al., 2004, Fujiwara et al. 2004,
338 Oth et al. 2011, Laurendeau et al. 2013). These limits ensure a broad frequency bandwidth for κ
339 calculations of at least 10 Hz per record, which reduces potential bias from local amplification
340 effects (Parolai and Bindi, 2004; Ktenidou et al. 2016). The arithmetic average of the resulting
341 κ_{r_AS} estimated from two orthogonal horizontal components is used because it is not affected by
342 the record azimuth and its implementation can reduce the variability in κ_{r_AS} caused by ground
343 motion directionality (Ji et al. 2020). However, a prescribed, fixed-frequency band does not
344 guarantee the most appropriate linear regression for the high-frequency spectral decay in all cases.
345 Thus, we further investigate the performance of the fixed-frequency window and the effects of the
346 frequency band selection for weak and strong ground motion records by comparing individual
347 κ_{r_AS} values estimated from a pre-determined fixed frequency window with their counterparts,
348 $\kappa_{r,auto}$, resulting from an automated algorithm which does account for the most appropriate linear
349 regression.
350
351 The automated procedure used in this paper follows a similar protocol as those presented in
352 Sonnemann, and Halldorsson (2017) and Pilz et al. (2019), which focus on finding an appropriate
353 frequency band ($[f_1, f_2]$) to describe the linear decay in the high frequency range over a relatively
354 broad frequency window. As part of the automated protocol, the minimum f_1 is selected as the
355 maximum value between $1.4f_0$, and $1.4fc$. To ensure a minimum frequency bandwidth of 10 Hz,
356 the maximum value of f_1 is 15 Hz and the minimum f_2 corresponds to (f_1 +10) Hz. With 0.5 Hz
357 increments in f_1 and f_2, f_1 is varied from the maximum value between $1.4f_0$ and $1.4f_c$ to 15 Hz, while
358 f_2 changes from (f_1+10) Hz to 25 Hz. Going through all the possible combinations of f_1 and f_2, the
359 frequency range with the minimum root mean square error over the frequency bandwidth is set as

the optimal frequency band. The errors are computed with the following equation after Pilz et al. (2019):

$$P = RMS \Big/ \sqrt{\Delta f} \tag{3}$$

Where Δf is the frequency bandwidth, and RMS is the root mean square error between the fitting line and smoothed FAS. The FAS is smoothed with the Konno-Ohmachi filter with a coefficient of 40 (Konno and Ohmachi, 1998). It should be noted that this automated procedure returns $\kappa_{r,auto}$ values associated with an appropriate regression for a broad frequency band. However, the changes of the FAS shape in high frequencies caused by site effects or soil nonlinearity (e.g., bumps or multiple linear trends) may not be properly accounted for by the automated algorithm.

Figure 6 compares κ_{r_AS} and $\kappa_{r,\ auto}$ for all selected ground motions at FKSH14, where overall similar κ_{r_AS} and $\kappa_{r,\ auto}$ estimates are observed and discrepancies are more significant at the ground surface than at depth. The remaining stations also show an acceptable agreement between the two methods at the surface and at depth. However, there are few records that show significant differences between κ_{r_AS} and $\kappa_{r,\ auto}$ (e.g., one surface record has κ_{r_AS} of about 0.025 s, while $\kappa_{r,\ auto}$, auto is almost 0.05 s). This reflects the variability of κ_r as a function of the frequency band selected. For example, there are 13% of records at AICH17 showing clear variations with the frequency band selection based on the coefficient of variation (COV) obtained for all frequency windows evaluated by the automatic procedure (i.e., COV larger than 0.15). Differences between κ_{r_AS} and $\kappa_{r,\ auto}$ are mainly caused by some empirical FAS shapes, for example, when multiple linear decaying trends are present in the high-frequency range. The latter cannot be captured by the single linear decay assumption within the κ-model. More research is needed to study how more

382 complex wave propagation effects in the high frequency range can be captured. Testing the
383 appropriateness of the κ-model as introduced by Anderson and Hough (1984) for these cases is
384 outside the scope of this study, but it constitutes an area of relevant future research.
385
386 Negative κ_{r_AS} values are excluded from this work. Overall, there are 14 of 20 stations with less
387 than 20% negative κ_{r_AS} values (i.e., arithmetic means of two horizontal components), and 1 of 20
388 stations with more than 50% negative κ_{r_AS} estimates. To further understand the observed negative
389 κ_{r_AS} values, the corresponding FAS are reinspected. These FAS generally show bumps or multiple
390 linear decays in high frequencies. The pre-determined frequency band used in this study is then
391 not able to capture the linear decay appropriately and leads to negative κ_{r_AS} values. Moreover,
392 amplifications at higher frequencies may also affect estimates of κ_{r_AS} and lead to negative values.
393 The original κ_r model (i.e., the linear decay of FAS in log-linear scale for high frequency ranges
394 per record proposed by Anderson and Hough, 1984), requires the site response at the site of interest
395 to be almost flat in the high frequency range. Complex in-situ site conditions that lead to high
396 frequency amplification (e.g., heterogeneities in the near-surface, and/or shallow impedance
397 contrasts) can challenge this simple linear decay model. Our observations suggest the need to
398 further explore the limitations and simplified assumptions of the Anderson and Hough (1984) κ_r
399 model for it to be applicable or extended to more complex environments and stronger ground
400 shaking. Accounting for the discrepancies between actual field conditions and assumptions
401 suggested by the Anderson and Hough (1984) κ model could reduce the large variability observed
402 in κ_{r_AS} estimates. Further research should focus on evaluating the limitations of the Anderson and
403 Hough (1984) model and its potential modification to capture more complex wave propagation
404 patterns in heterogeneous media, especially near the surface. In this work, such an investigation is

not included, but future efforts of the authors envision the assessment of negative κ_{r_AS} estimates observed in this work as a first step to improve the existing κ model.

κ_0-model

κ_{r_AS} is generally modeled with contributions from a site-specific component (κ_0), a path component (κ_R), and a source component (κ_s). The source component, κ_s, is often assumed to be negligible and its contribution is reduced by using a dataset with sufficient records (Van Houtte et al. 2011, Ktenidou et al. 2014). A linear distance-dependency model is commonly applied to capture the path component κ_R, which represents source-to-site effects or regional attenuation (Hough et al. 1988, Anderson, 1991, Ktenidou et al. 2013, Boore and Campbell, 2017). Thus, the most commonly accepted model is described below:

$$\kappa_{r\_AS} = \kappa_0 + \kappa_R \times R_e \quad (4)$$

where κ_0 and κ_{r_AS} are in units of time (s), κ_R is in units of second per kilometer (s/km) and R_e refers to epicentral distance in km. This model is valid when a unique source-to-site path is assumed for each record along with a homogeneous and frequency-independent seismic quality factor Q (Knopoff 1964). In this paper, the assumption of a unique source-to-site path is supported by using ground motions with R_e less than 150 km (e.g., Palmer and Atkinson 2020, Cabas et al. 2017, Ktenidou et al. 2013). In addition, ground motions whose travel path crosses Japan's volcanic belt are not included in our database to minimize the likelihood of seismic waves propagating through regions with varying Q values (Pei et al. 2009, Nakano et al. 2015).

The model described by Equation (4) is straightforward to apply when only surface linear ground motion datasets are used. However, the incorporation of nonlinear and borehole ground motions

adds complexity to the estimation of regional attenuation as captured by κ_R. In this paper, we assume that soil nonlinearity is triggered near the surface, which is consistent with previous studies showing that nonlinear behavior occurs mostly in the superficial soil layers (i.e., Régnier et al., 2013; Bonilla et al., 2019; Qin et al., 2020). Thus, nonlinear soil behavior is treated as a site contribution rather than a path contribution, and we assume the regional attenuation to be identical for linear and nonlinear ground motions recorded at the ground surface and at depth.

Analogous to the formulation suggested by Douglas et al. (2010) for soil and rock sites, we propose a model based on Equation (4), which includes linear and nonlinear surface and borehole records:

$$\kappa_{r\_AS} = N_1\kappa_{0\_depth} + N_2\kappa_{0\_lin\_sur} + N_3\kappa_{0\_nl\_sur} + N_4\kappa_{0\_tran\_sur} + \kappa_R \times R_e \quad (5)$$

where κ_{0_depth} is the site-specific κ_0 at depth (i.e., depth of borehole sensor), and $\kappa_{0\_lin\_sur}$, $\kappa_{0\_tran\_sur}$ and $\kappa_{0\_nl\_sur}$ are the site-specific linear, transitional and nonlinear κ_0 at the surface. The coefficients N_1, N_2, N_3, and N_4 are defined as follows:

$$N_1 = \begin{cases} 1 & for\ dataset\ at\ depth \\ 0 & otherwise \end{cases}$$

$$N_2 = \begin{cases} 1 & for\ linear\ dataset\ at\ surface \\ 0 & otherwise \end{cases}$$

$$N_3 = \begin{cases} 1 & for\ nonlinear\ dataset\ at\ surface \\ 0 & otherwise \end{cases}$$

$$N_4 = \begin{cases} 1 & for\ transitional\ dataset\ at\ surface \\ 0 & otherwise \end{cases}$$

The parameter N_4 in Equation (5) only takes a value of 1 when ground motions classified as transitional are considered independently and not as part of the linear or nonlinear datasets. That means that when transitional ground motions are excluded from analysis (i.e., AP1, see Table 2) or included into either the linear (i.e., AP2, see Table 2) or nonlinear (i.e., AP3, see Table 2) datasets, the coefficient N_4 will be equal to zero.

Results and Discussion

Effects of soil nonlinearity on empirical κ_{r_AS}

First, we study the influence of soil nonlinearity on κ_{r_AS} estimates per record at each site. It should be noted that soil nonlinearity is commonly triggered at shallower soil layers (Régnier et al. 2013), so we only focus on surface records in this section. Figure 7 depicts calculated κ_{r_AS} values at the surface against the corresponding $I_{\gamma,0}$ values at FKSH14 (V_{s30} = 237 m/s) and MYGH10 (V_{s30} = 348 m/s). As described in Equation (4), κ_{r_AS} is affected by both local site conditions and path effects in the context of a linear-elastic deformation analysis. Hence, the colorbar in Figure 7 represents varying epicentral distances, and the sizes of markers represent the corresponding PGA_{rotD50}. An overall increasing trend of κ_{r_AS} with increasing intensity of ground shaking (either evidenced by increased PGA or $I_{\gamma,0}$ values) is observed at FKSH14 for events that share similar epicentral distances. A slightly decreasing trend is observed for short-distance records with R_e less than about 50 km and high PGA_{rotD50}. However, κ_{r_AS} values corresponding to those shorter distance and higher PGA_{rotD50} events (i.e., the largest circles in Figure 7a) are larger than their counterparts for low-intensity motions (i.e., the smallest circles in Figure 7a) regardless of the R_e. To the best knowledge of the authors, this observation has not been reported before and could be associated with the depth of influence of κ_r. Variations in κ due to strong nonlinear effects may be a function of a more significant contribution of the site to the overall attenuation, which may not be necessarily the case for smaller amplitude events. There might be several mechanisms of attenuation combined, and their contributions as captured by κ need to be further investigated. Similar trends are observed at other seven sites with V_{s30} less than 400 m/s, which include AICH17,

CHBH13, FKSH11, IBRH20, IWTH26, MYGH07, and TCGH16, and at KMMH12 with V_{s30} greater than 400 m/s.

The increasing κ_{r_AS} trend with increasing PGA_{rotD50} and $I_{\gamma,0}$ is not as significant at MYGH10 (Figure 7b), which has relatively stiffer site conditions than FKSH14. Either no correlation or a slightly decreasing trend is found at other stiff sites with V_{s30} greater than 400 m/s (i.e., FKSH21, NIGH12, NGNH29, NIGH07, KMMH01, and IBRH16), and at four softer sites with V_{s30} between 300 and 400 m/s (i.e., IWTH21, FKSH18, FKSH19, and IBRH17). We note that the number of available nonlinear records for the R_e ranges at the sites where the decreasing trend is observed is rather limited. Additional nonlinear records at those sites are necessary (i.e., stronger intensity ground motions) to further evaluate the contributing factors to a potential decreasing trend in κ_{r_AS} values. However, in general, we observe that positive correlations between κ_{r_AS} and the intensity of ground shaking are more significant at softer sites (e.g., TCGH16 with V_{s30} of 213 m/s) than at stiffer sites (e.g., KMMH12 with V_{s30} of 408 m/s). These data support that the onset of soil nonlinearity can affect κ_{r_AS} estimates, but such influence is station-dependent. The level of soil nonlinearity can be unique at each site (for a similar intensity of ground shaking) because of the characteristics of shallow geologic structures (e.g., differences in velocity gradients and seismic impedance contrasts) and the location of low shear-wave velocity layers. Thus, subsurface conditions can play a key role on the effects of nonlinearity on κ_{r_AS}. We observe the same patterns shown in Figure 7 when using our results from the automated procedure to compute $\kappa_{r,auto}$.

Effects of soil nonlinearity on the empirical κ_0-model

Linear, transitional, and nonlinear ground motion datasets are used in this section to evaluate the κ_0-model beyond the linear-elastic regime. We explore four approaches (i.e., AP1 to AP4) to incorporate records within the transitional dataset into the κ_0-model presented in Equation (5). Table 2 summarizes how the identified linear, transitional, and nonlinear datasets are used to estimate $\kappa_{0\_lin\_sur}$ and $\kappa_{0\_nl\_sur}$.

Figures 8 and 9 present the resulting κ_0 models from each approach at FKSH14 and MYGH10, respectively. Figure 8 shows that κ_{r_AS} and κ_0 values corresponding to the nonlinear ground motions (regardless of the selected approach to construct the nonlinear dataset) are larger than their linear counterparts at FKSH14. However, results at the stiffer station presented in Figure 9 show little disagreement between κ_{r_AS} and κ_0 values corresponding to the linear and nonlinear motions (regardless of the approach to construct each dataset).

Variations in $\kappa_{0\_lin\_sur}$ estimates are observed as a function of the approach considered to construct the linear datasets (see specific values in Table 3 for FKSH14 and MYGH10, the results for other selected stations are available in the electronic supplement). Similarly, variations in $\kappa_{0\_nl\_sur}$ values are also found across the different approaches to define the nonlinear datasets. At FKSH14 (Figure 8), $\kappa_{0\_lin\_sur}$ estimates are more variable as a function of the dataset definitions (with a maximum difference of 15.83% across approaches AP1 to AP4), compared to $\kappa_{0\_nl\_sur}$ values (with a maximum difference of 5.10%). In addition, Figure 8 (d) shows that data points corresponding to the transitional dataset are more compatible with their counterparts within the nonlinear dataset, which may indicate that at FKSH14, the level of nonlinearity induced by the transitional dataset is

516 closer to that induced by the ground motions in the nonlinear dataset. Other study sites such as
517 AICH17 (V_{s30} = 314 m/s) and IWTH21 (V_{s30} = 521 m/s) also show that $\kappa_{0\_lin\_sur}$ estimates are more
518 sensitive to dataset selections. In contrast, variations of $\kappa_{0\_lin\_sur}$ and $\kappa_{0\_nl\_sur}$ across datasets at
519 MYGH10 (Figure 9) are small, with maximum differences of only 1.56% and 2.53%, respectively.
520 Large differences in $\kappa_{0\_nl\_sur}$ estimates across datasets are observed at eight sites, but the limited
521 number of nonlinear records at some of those sites may be the main contributing factor (e.g., there
522 are only six nonlinear records at IWTH21, which results in a maximum difference of 47.05% for
523 $\kappa_{0\_lin\_sur}$ and 11.17% for $\kappa_{0\_nl\_sur}$). Adding transitional records to either the linear or the nonlinear
524 dataset at such sites can bias the regression model. In general, differences in the κ_0–model as a
525 function of the selected dataset are observed in 45% of our study sites (with differences in $\kappa_{0\_lin\_sur}$
526 or $\kappa_{0\_nl\_sur}$ values greater than 10%). This is a relevant observation because it demonstrates the
527 importance of selecting appropriate ground motions even for typical κ_0 estimations (i.e., in the
528 linear-elastic regime) at a given site.
529
530 Our findings suggest that the development of a κ_0-model beyond the linear-elastic regime requires
531 an evaluation of the definition of what constitutes linear and nonlinear ground motion datasets.
532 The identification of transitional ground motion datasets in this study allows us to assess which
533 records provide estimates of κ_{r_AS} that are closer to either the linear or the nonlinear behavior at
534 different sites. Differences in behavior triggered by the records within the transitional database
535 may be caused by unique local site conditions (i.e., the level of soil nonlinearity developed at each
536 site) or by limitations of the simplified definition used herein to classify transitional records (i.e.,
537 as a function of PGA and I_γ). Identifying appropriate linear and nonlinear datasets for κ_{r_AS}
538 estimations requires further research to provide consistent models of near-surface attenuation that

539 can more effectively be implemented from small to large shear strains. However, the site-specific
540 response at a site of interest may impose challenges in determining appropriate dataset
541 classifications based on a simple, generalized criterion.
542
543 Figure 10 provides ratios of $\kappa_{0\_nl\_sur}/\kappa_{0\_lin\_sur}$ at the 20 study sites against the corresponding time-
544 average V_s value in the top 5 m (V_{s5}), 10 m (V_{s10}), and 30 m (V_{S30}). The ratios are computed based
545 on the AP3 and AP4 approaches to construct linear and nonlinear datasets (Table 2). Larger ratios
546 are observed at softer sites regardless of the dataset chosen (i.e., AP3 and AP4) for the κ_0-model.
547 Differences between κ_0 values in the linear and nonlinear regimes seem to be reconciled at sites
548 with higher V_{s5} (> 300 m/s), V_{s10} (> 300 m/s) and V_{s30} (> 400 m/s) values, where the ratios fluctuate
549 more closely around unity particularly when using AP3. The trend of increasing ratios of
550 $\kappa_{0\_nl\_sur}/\kappa_{0\_lin\_sur}$ with softer site conditions is better captured by V_{s5} and V_{s10} than by V_{s30}, because
551 soil nonlinearity is more likely triggered at shallower and softer layers (Régnier et al. 2013). Hence,
552 lower V_s layers may dominate soil nonlinearity effects on κ_0. Thus, site proxies that can
553 characterize such near-surface layers may be more informative when evaluating nonlinear soil
554 effects on κ_0.
555
556 When grouping transitional and nonlinear ground motions (i.e., AP3), most stations result in ratios
557 of $\kappa_{0\_nl\_sur}/\kappa_{0\_lin\_sur}$ larger than one, which can be interpreted as the signature of soil nonlinearity
558 on the near-surface attenuation estimates (i.e., near-surface attenuation increases with increasing
559 deformations as soil nonlinearity is triggered). These findings are consistent with the behavior of
560 material damping ratio observed in dynamic laboratory testing of soils (i.e., increased damping
561 ratio with increasing shear strain; Darendeli 2001; Menq 2003; Ishibashi and Zhang 1993). When

562 treating linear, transitional, and nonlinear datasets independently (i.e., AP4), there are 12 sites with
563 ratios larger than one. The instances where ratios of $\kappa_{0\_nl\_sur}/\kappa_{0\_lin\_sur}$ are lower than one may result
564 from the limited nonlinear records available at those sites coupled with the uncertainties associated
565 with $\kappa_{0\_lin\_sur}$ (e.g., Ji et al., 2020).
566
567 Overall, the variations observed in the $\kappa_{0\_nl\_sur}/\kappa_{0\_lin\_sur}$ ratio support our hypothesis that soil
568 nonlinearity plays a role on the estimates of near-surface attenuation from recorded ground
569 motions. This effect is station-dependent, and further research is needed to identify the most
570 appropriate parameter or vector of parameters capable of capturing the influence of nonlinear soil
571 behavior on near-surface attenuation. Moreover, the relatively weaker correlation between V_{s30}
572 and the $\kappa_{0\_nl\_sur}/\kappa_{0\_lin\_sur}$ ratio evidences the challenges in connecting site conditions and soil
573 nonlinearity via a single site parameter. Multiple parameters that can describe attenuation and
574 impedance effects from the shallow and deep geologic structures should be investigated. The
575 $\kappa_{0\_nl\_sur}/\kappa_{0\_lin\_sur}$ ratio corresponding to IWTH21 (V_{s30} = 521 m/s) is not shown in Figure 10 because
576 it is very large (i.e., approximately 1.8). This observation may result from uncertainties associated
577 with κ_{r_AS} values propagating to estimates of κ_0 when the fixed frequency band approach is applied
578 for all records without consideration of the optimal linear decay trend. In fact, the corresponding
579 $\kappa_{0\_nl\_sur}/\kappa_{0\_lin\_sur}$ ratio when implementing the automated procedure is approximately 0.90 for this
580 station. Finally, Figure 10 shows less scatter in $\kappa_{0\_nl\_sur}/\kappa_{0\_lin\_sur}$ ratios when using datasets defined
581 by AP3. In addition, using AP3 results in ratios either larger than one or approaching one for most
582 stations (i.e., only FKSH19 and KMMH01 results in a ratio lower than unity), which is consistent
583 with our conceptual basis for increased attenuation with the onset of nonlinear soil behavior.

584 Therefore, we adopt the AP3 approach (which includes transitional records into nonlinear dataset)
585 to evaluate predictions of near-surface attenuation in the next section of this paper.
586
587 **Effects of soil nonlinearity on predicted near-surface attenuation**
588 Site-specific $\kappa_{0\_lin\_sur}$ or $\kappa_{0\_nl\_sur}$ values from Equation (5) allow for the comparison of empirical
589 estimates of near-surface attenuation, but these two parameters represent the average attenuation
590 of all records in linear and nonlinear regimes. Thus, in this section, we introduce the predicted
591 near-surface attenuation at zero-distance (κ_{0_pred}), which is expected to capture the attenuation
592 contributed by the superficial soil layers per event by removing the path contributions from κ_{r_sur}.
593 κ_{0_pred} is modeled as:
594
$$\kappa_{0\_pred} = \kappa_{r\_AS\_sur} - R_e \bullet \kappa_R \quad (6)$$

595 where $\kappa_{r\_AS\_sur}$ refers to the individual κ_{r_AS} value for a surface ground motion, and the path-
596 component, κ_R, corresponds to the values derived with Equation (5) at each site of interest. We
597 assume that by removing the effect of the path-component κ_R from $\kappa_{r\_AS\_sur}$ values per record, the
598 remaining κ_{0_pred} becomes an approximation to the attenuation contributed by the shallower
599 sedimentary deposits per event. Thus, we can explore how the near-surface attenuation changes
600 with the various input ground motion amplitudes at the site of interest.
601
602 Figure 11 provides comparisons between $\kappa_{0\_pred,}$ ground shaking intensity, and deformation as
603 captured by PGA_{rotD50} and $I_{\gamma,0}$ at FKSH14 and MYGH10. Both colors and sizes of markers
604 represent the PGA_{rotD50} values per record. The red dashed-lines result from a local regression model
605 characterizing the κ_{0_pred} versus $I_{\gamma,0}$ data. Triangles and circles represent the linear and nonlinear

606 ground motions (identified with AP3), respectively. Values of κ_{0_pred} first increase and then
607 decrease with increasing PGA_{rotD50} and $I_{\gamma,0}$ at FKSH14. This behavior is also observed at other 7
608 sites (i.e., AICH17, CHBH13, FKSH11, IWTH26, KMMH12, MYGH07, TCGH16). Even with
609 the decreasing trend for large $I_{\gamma,0}$, κ_{0_pred} is still generally higher than its counterpart in the linear
610 regime (i.e., the means of linear and nonlinear κ_{0_pred} are 0.050 sec and 0.0605 sec, respectively).
611 Overall, κ_{0_pred} values at FKSH14 corresponding to larger deformations and higher PGA_{rotD50} are
612 larger than those corresponding to weaker ground motions. In contrast, only a weak correlation to
613 the intensity of ground shaking and deformation in situ is observed at MYGH10. These results are
614 consistent with our estimations of κ_r shown in Figure 7. Soil nonlinear behavior can influence
615 near-surface attenuation as captured by κ_r and κ_0, and local site conditions may play a key role in
616 this process. The remaining approaches explored in this study (i.e., AP1, AP2, and AP4) provide
617 similar results as those shown in Figure 11.
618
619 Figure 12 compares the probability distribution of κ_{0_pred} values from the linear and nonlinear
620 datasets (AP3 case) at FKSH14 and MYGH10. The resulting κ_{0_pred} values are fitted with a
621 Gaussian distribution and the corresponding probability density functions (PDFs) are represented
622 by red lines. A shift to the right (i.e., toward larger κ_{0_pred} values) of the theoretical PDF is observed
623 at FKSH14 as ground motions from the linear and nonlinear datasets are considered. The mean
624 κ_{0_pred} estimates change from 0.05 s for the linear dataset to 0.0605 s for the nonlinear dataset at
625 FKSH14 (i.e., a difference of 21%). In contrast, the variation of mean κ_{0_pred} between linear and
626 nonlinear datasets at MYGH10 is 4%. Most of our study sites have either a significant increase in
627 their mean κ_{0_pred} when using the nonlinear dataset (i.e., an increase of more than 20%) or only a
628 slight increase. There are only 4 stations that show a decrease in their mean κ_{0_pred} values with

629 respect to the linear dataset when using the nonlinear one (i.e., FKSH19, KMMH01, NIGH07, and
630 NIGH12). Statistical hypothesis tests (i.e., t-test) are conducted to analyze whether there is a
631 statistically significant difference between the means of linear and nonlinear κ_{0_pred} distributions.
632 Considering a critical value of 5%, p-values at each station are shown in Table 4. Nine out of 20
633 stations display statistically significant differences between their mean κ_{0_pred} corresponding to the
634 linear and nonlinear datasets. Table 4, Figures 11 and 12 show that soil nonlinear behavior can
635 affect κ_{0_pred} at the sites selected in this study, although this influence is station-dependent. At the
636 stations that display apparent effects of nonlinearity on κ, an increasing trend in predicted near-
637 surface attenuation with increasing ground shaking intensity and/or increasing deformation is
638 observed.

639 **Conclusions**

640 In this work, we investigated the influence of soil nonlinear behavior on κ_{r_AS} values per record
641 and site-specific κ_0 estimates at 20 stations selected from the KiK-net database. To avoid potential
642 bias on our results due to the calculation process, we also examined the effects of the frequency
643 band selection on κ_{r_AS} estimates, and the differences between using the S-wave window or the
644 entire time series FAS. We compared results from a predetermined fixed-frequency window
645 approach with an automated procedure that considers multiple frequency windows. The latter is
646 capable of finding the optimal frequency band per record for all records at each site. The selection
647 of a common, fixed and broader frequency band for κ_{r_AS} estimations reduced the scatter and bias
648 in the data, while providing reasonable estimations of κ_{r_AS}. On the other hand, values of κ_{r_AS}
649 computed from the S-wave window FAS were reasonably similar to their counterparts based on
650 the entire time series FAS. Hence, the analyses presented in this paper were conducted with κ_r

values estimated by the fixed-frequency band approach and the FAS corresponding to the entire time series.

A consistent identification of ground motions that trigger nonlinear behavior in sedimentary deposits is also necessary to quantify near-surface attenuation beyond the linear-elastic regime. Based on the examination of an in-situ stress-strain proxy, namely the correlation between PGA_{rotD50} and $I_{\gamma,0}$, we found that the variation of shear strains with ground shaking intensity at the onset of nonlinear soil behavior is site-specific. A unique threshold for a single parameter, whether it is PGA_{rotD50} or $I_{\gamma,0}$, was not able to capture the onset of soil nonlinearity at our study sites in a consistent manner across all sites. Hence, we proposed a hybrid method to classify linear and nonlinear ground motions considering both, PGA_{rotD50} and $I_{\gamma,0}$, which resulted in linear, transitional, and nonlinear datasets at each site.

Increasing κ_{r_AS} values with increasing PGA_{rotD50} or $I_{\gamma,0}$ for ground motions with similar epicentral distances were observed at about half of our study sites. This trend was more consistently observed at softer sites. Additionally, we found that κ_0-models could be biased by the definition of linear and nonlinear ground motion datasets. Hence, we studied the effects of ground motion categorization and proposed a hybrid classification scheme for linear and nonlinear records. We defined transitional ground motions as those associated with soil behavior between the linear-elastic and nonlinear regimes. Even though more research is necessary to define robust classification schemes for linear and nonlinear ground motions, we observed that including the transitional motions into the nonlinear dataset reduced the variability associated with κ estimations at our study sites.

Our results also revealed differences between $\kappa_{0\_lin\_sur}$ (i.e., κ_0 corresponding to the linear-elastic regime) and $\kappa_{0\_nl\_sur}$ (i.e., κ_0 for the nonlinear regime) at most sites when implementing the κ_0-model using ground motions classified by AP3 (which includes transitional records into the nonlinear dataset). Such differences were more prevalent among softer sites. Site parameters such as V_{s5}, V_{s10}, and V_{s30} were used in this study to investigate the influence of soil conditions on the effects of nonlinearity on κ_0. Considering that high frequencies have short wavelengths, and that nonlinear soil behavior is triggered in low velocity layers more often located at a shallow depth, site proxies such as V_{s5} and V_{s10} may be more informative than V_{s30} when assessing effects of nonlinearity on κ. For instance, large V_{s30} values do not imply that all near-surface layers have a large $V_{s.}$ The ratio of $\kappa_{0\_nl\_sur}$ and $\kappa_{0\_lin\_sur}$ decreases and approaches one for increasing V_{s5}, V_{s10}, and V_{s30}, when using the AP3 method to define nonlinear ground motion datasets.

The hypothesis posed and tested in this paper focused on the effects of ground shaking intensity on induced shear strains in sedimentary deposits and associated consequences on the attenuation experienced by seismic waves (particularly in the high frequency range). In general, we find that soil nonlinear behavior can affect estimates of κ_{r_AS} and κ_0, but our results show that this influence is station-dependent. This is reasonable because the wave propagation of short wavelength waves is highly affected by heterogeneities in the soil or rock, local geologic structures, and topography. Moreover, the level of soil nonlinearity can be distinct at a given site (even when site parameterizations such as V_{s30} are similar and the considered intensity of ground shaking is also similar) because of the complexities of the in situ subsurface conditions (e.g., differences in velocity gradients and seismic impedance contrasts). We note that 2D/3D site effects may affect

ground motions recorded at six of our stations. The influence of soil nonlinearity on κ values computed at these stations (i.e., AICH17, CHBH13, FKSH21, IBRH20, KMMH01, KMMH12; based on the classification of Thompson et al. 2012 and Pilz and Cotton 2019) may be masked by the combined effects of wave scattering and topographic effects. Further research is necessary to evaluate the contributions of the aforementioned mechanisms on κ estimates at stations subjected to 2D/3D site effects. Likewise, future work should focus on collecting and analyzing additional strong ground motion data to identify local site conditions more conducive to generate significant changes in near-surface attenuation as captured by κ_0 when nonlinear soil behavior is triggered.

Complexities in the wave propagation phenomenon driven by scattering effects and amplification in the high-frequency range can result in negative estimates of κ_r. In this study, we obtained negative κ_{r_AS} estimates when multiple linear decaying trends, bumps, and high frequency amplifications affected the corresponding FAS spectral shape. The identification of multiple linear decays in the high-frequency range supports previous work on the bias in κ_{r_AS} associated with the selection of the frequency band. The bumps and amplifications in the high frequencies present in the FAS of some of the ground motions in our database hint that the site response may not be approximately flat within the frequency range of interest for κ_{r_AS} calculation. Considering that a flat site response is one of the assumptions of the Anderson and Hough (1984) κ-model, further research is needed to overcome this limitation at sites where this is not the case. This work not only provides evidence of the need to understand and quantify κ in both, the linear and nonlinear regimes, but it also presents the limitations of the current κ-model when it comes to characterizing attenuation when conditions deviate from the original assumptions embedded in the Anderson and Hough (1984) model.

Data and Resources

Accelerograms and geotechnical data are downloaded from the KiK-net network at http://www.kyoshin.bosai.go.jp (last accessed May 2020). The earthquake information is available from F-net network at http://www.fnet.bosai.go.jp/top.php (last accessed May 2020). The supplemental material to this article includes two tables and three figures. The tables provide the κ_0-model results when using the datasets defined by AP1, AP2, AP3, and AP4, and the κ_{0_pred} results estimated with datasets defined by AP3. The three sets of figures presented depict the results corresponding to our 20 stations as follows:

- Surface PGA_{rotD50} against $I_{\gamma,0}$ (i.e., results analogous to those presented in Figure 4 for MYGH10).
- Surface κ_{r_AS} estimates and their corresponding PGA_{rotD50}, $I_{\gamma,0}$ and R_e values for selected ground motions at each study site (i.e., results analogous to those presented in Figure 7 for FKSH14 and MYGH10).
- Estimated surface κ_{0_pred} and their corresponding ground shaking intensity and in situ deformation characterized by PGA_{rotD50} against $I_{\gamma,0}$, respectively (i.e., results analogous to those presented in Figure 11 for FKSH14 and MYGH10).

Acknowledgements

The authors would like to appreciate that the National Research Institute for Earth and Disaster Prevention (NIED) provides the ground motion and site information. The authors acknowledge Dr. Adrian Rodriguez-Marek and Mahdi Bahrampouri for sharing their processed dataset. We also are thankful to Associate Editor Stefano Parolai and two anonymous reviewers for the useful comments. This work was sponsored by the U.S. Geological Survey under Grant Number

743 G19AP00058 and the NCSU Internationalization Seed Grant. The views and conclusions
744 contained in this document are those of the authors and should not be interpreted as representing
745 the opinions or policies of the U.S. Geological Survey.
746

747 **Reference**

748 Anderson, J. G., & Hough, S. E. (1984). A model for the shape of the Fourier amplitude spectrum
749 of acceleration at high frequencies. *Bull Seismol Soc Am*. **74**, no. 5, 1969-1993.

750 Anderson, J.G. (1991). A preliminary descriptive model for the distance dependence of the spectral
751 decay parameter in southern California. *Bull Seismol Soc Am*. **81**, no. 6, 2186-2193.

752 Al Atik, L., Kottke, A., Abrahamson, N. and Hollenback, J., (2014). Kappa (κ) scaling of ground-
753 motion prediction equations using an inverse random vibration theory approach. Bulletin
754 of the Seismological Society of America, 104, no. 1, 336-346.

755 Aoi, S., T. Kunugi, and H. Fujiwara (2004). Strong-motion seismograph network operated by
756 NIED: K-NETand KiK-net, J. Japan Assoc. Earthq.Eng. 4, no. 3, 65–74.

757 Bahrampouri, M., Rodriguez-Marek, A., Shahi, S., & Dawood, H. (2020). An update database for
758 ground motion parameters for KiK-net records. Earthquake Spectra.

759 Bonilla, L.F., Tsuda, K., Pulido, N., Régnier, J. and Laurendeau, A., 2011. Nonlinear site response
760 evidence of K-NET and KiK-net records from the 2011 off the Pacific coast of Tohoku
761 Earthquake. Earth, planets and space, 63(7), p.50.

762 Bonilla, L.F., Guéguen, P. and Ben-Zion, Y., 2019. Monitoring Coseismic Temporal Changes of
763 Shallow Material during Strong Ground Motion with Interferometry and
764 AutocorrelationMonitoring Coseismic Temporal Changes of Shallow Material during

765 Strong Ground Motion. Bulletin of the Seismological Society of America, 109(1), pp.187-
766 198.

767 Bonilla, L.F. and Ben-Zion, Y., 2020. Detailed space-time variations of the seismic response of
768 the shallow crust to small earthquakes from analysis of dense array data. Geophysical
769 Journal International.

770 Boore, D.M., 2003. Simulation of ground motion using the stochastic method. *Pure and applied*
771 *geophysics*, 160(3-4), pp.635-676.

772 Boore, D.M. and Bommer, J.J., 2005. Processing of Strong-Motion Accelerograms: Needs,
773 Options and Consequences. Soil Dynamics and Earthquake Engineering, 25(2), 93-115.

774 Boore, D. M. (2010). Orientation-independent, nongeometric-mean measures of seismic intensity
775 from two horizontal components of motion. *Bull Seismol Soc Am*. 100, no. 4, 1830-1835.

776 Boore, D.M. and Campbell, K.W., 2017. Adjusting central and eastern North America ground-
777 motion intensity measures between sites with different reference-rock site conditions.
778 Bulletin of the Seismological Society of America, 107(1), pp.132-148.

779 Campbell, K.W., 2003. Prediction of strong ground motion using the hybrid empirical method and
780 its use in the development of ground-motion (attenuation) relations in eastern North
781 America. Bulletin of the Seismological Society of America, 93(3), pp.1012-1033.

782 Cabas, A., Rodriguez-Marek, A., & Bonilla, L. F. (2017). Estimation of Site-Specific Kappa (κ0)-
783 Consistent Damping Values at KiK-Net Sites to Assess the Discrepancy between
784 Laboratory-Based Damping Models and Observed Attenuation (of Seismic Waves) in the
785 Field. *Bull Seismol Soc Am*. **107**, no. 5, 2258-2271.

786 Chandra, J., Guéguen, P. and Bonilla, L.F., 2014. Application of PGV/VS proxy to assess
787 nonlinear soil response–from dynamic centrifuge testing to Japanese K-NET and KiK-net
788 data. In Second European Conference on Earthquake Engineering and Seismology,
789 Istanbul Aug (pp. 25-29).

790 Chandra, J., Guéguen, P., Steidl, J.H. and Bonilla, L.F., 2015. In situ assessment of the G–γ curve
791 for characterizing the nonlinear response of soil: Application to the Garner Valley
792 downhole array and the wildlife liquefaction array. Bulletin of the Seismological Society
793 of America, 105(2A), pp.993-1010.

794 Chandra, J., Gueguen, P. and Bonilla, L.F., 2016. PGA-PGV/Vs considered as a stress–strain
795 proxy for predicting nonlinear soil response. Soil dynamics and earthquake engineering, 85,
796 pp.146-160.

797 Darragh, R.B. and Shakal, A.F., 1991. The site response of two rock and soil station pairs to strong
798 and weak ground motion. Bulletin of the Seismological Society of America, 81(5),
799 pp.1885-1899.

800 Darendeli M. B. (2001). Development of a new family of normalized modulus reduction and
801 material damping curves, Ph.D. Thesis, University of Texas at Austin, Austin, Texas.

802 Dimitriu, P., Theodulidis, N., Hatzidimitriou, P., & Anastasiadis, A. (2001). Sediment non-
803 linearity and attenuation of seismic waves: a study of accelerograms from Lefkas, western
804 Greece. *Soil Dynam Earthquake Eng*. **21**, no.1, 63-73.

805 Durward, J.A., Boore, D.M., Joyner, W.B., Durward, J.A., Boore, D.M. and Joyner, W.B., 1996.
806 The amplitude dependence of high-frequency spectral decay: constraint on soil

807 nonlinearity. In Proc, of the International Workshop on Site Response Subjected to Strong
808 Earthquake Motions (pp. 82-103).

809 Drouet, S., F. Cotton, and P. Gueguen (2010). VS30, κ, regional attenuation and Mw from
810 accelerograms: Application to magnitude 3–5 French earthquakes, Geophys. J. Int. 182,
811 880–898.

812 Douglas, J., Gehl, P., Bonilla, L.F. and Gélis, C., (2010). A κ model for mainland France. Pure
813 Appl Geophys. 167, no.11, 1303-1315.

814 Douglas, J. and Boore, D.M., 2011. High-frequency filtering of strong-motion records. Bulletin of
815 Earthquake Engineering 9(2), 395-409.

816 Edwards, B., Ktenidou, O.J., Cotton, F., Abrahamson, N., Van Houtte, C. and Fäh, D., (2015).
817 Epistemic uncertainty and limitations of the κ 0 model for near-surface attenuation at hard
818 rock sites. *Geophys J Int.* **202**, no. 3, 1627-1645.

819 Fujiwara, H., S. Aoi, T. Kunugi, and S. Adachi (2004). Strong-motion observation networks of
820 NIED: K-NETand KiK-net, National Research Institute for Earth Science and Disaster
821 Prevention.Garcia, D., Wald, D. J., & Hearne, M. G. (2012). A global earthquake
822 discrimination scheme to optimize ground-motion prediction equation selection. Bull
823 Seismol Soc Am. 102, no.1, 185-203.

824 Guéguen, P., Bonilla, L.F. and Douglas, J., 2019. Comparison of Soil Nonlinearity (In Situ Stress–
825 Strain Relation and G/Gmax Reduction) Observed in Strong-Motion Databases and
826 Modeled in Ground-Motion Prediction EquationsComparison of Soil Nonlinearity
827 Observed in Strong-Motion Databases and Modeled in GMPEs. Bulletin of the
828 Seismological Society of America, 109(1), pp.178-186.

829 Hough, S.E., Anderson, J.G., Brune, J., Vernon III, F., Berger, J., Fletcher, J., Haar, L., Hanks, L.
830 and Baker, L., 1988. Attenuation near Anza, California. Bulletin of the Seismological
831 Society of America, 78(2), pp.672-691.

832 Idriss, I.M., Dobry, R.U. and Sing, R.D., 1978. Nonlinear behavior of soft clays during cyclic
833 loading. *Journal of geotechnical and geoenvironmental engineering*, 104.

834 Ishibashi, I. and Zhang, X., 1993. Unified dynamic shear moduli and damping ratios of sand and
835 clay. Soils and foundations, 33(1), pp.182-191.

836 Ji, C., Cabas, A., Cotton, F., Pilz, M. and Bindi, D., 2020. Within-Station Variability in Kappa:
837 Evidence of Directionality Effects. Bull Seismol Soc Am., 110(3), pp.1247-1259.

838 Knopoff, L. (1964). Q, Rev. Geophys. 2, no. 4, 625–660.

839 Ktenidou, O. J., Gélis, C., & Bonilla, L. F. (2013). A study on the variability of kappa (κ) in a
840 borehole: Implications of the computation process. *Bull Seismol Soc Am*. **103**, no.2A, 1048-
841 1068.

842 Ktenidou, O. J., Cotton, F., Abrahamson, N. A., & Anderson, J. G. (2014). Taxonomy of κ: A
843 review of definitions and estimation approaches targeted to applications. *Seismol Res Lett*.
844 **85**, no.1, 135-146.

845 Ktenidou, O.J., Abrahamson, N.A., Drouet, S. and Cotton, F., (2015). Understanding the physics
846 of kappa (κ): Insights from a downhole array. Geophys J Int. 203, no. 1, 678-691.

847 Ktenidou, O.J., Abrahamson, N., Darragh, R. and Silva, W., 2016. A methodology for the
848 estimation of kappa (κ) from large datasets, example application to rock sites in the NGA-
849 East database, and implications on design motions. PEER Report 2016, 1.

850 Konno, K. and Ohmachi, T., 1998. Ground-motion characteristics estimated from spectral ratio
851 between horizontal and vertical components of microtremor. Bulletin of the Seismological
852 Society of America, 88(1), pp.228-241.

853 Laurendeau, A., Cotton, F., Ktenidou, O. J., Bonilla, L. F., & Hollender, F. (2013). Rock and stiff-
854 soil site amplification: Dependency on VS 30 and kappa (κ 0). Bull Seismol Soc Am. 103,
855 no. 6, 3131-3148.

856 Lacave-Lachet, C., Bard, P.Y., Gariel, J.C. and Irikura, K., 2000. Straightforward methods to
857 detect non-linear response of the soil. Application to the recordings of the Kobe earthquake
858 (Japan, 1995). Journal of seismology, 4(2), pp.161-173.

859 Menq, F.Y., (2003). Dynamic properties of sandy and gravelly soils , Ph.D. Thesis, University of
860 Texas at Austin, Austin, Texas.

861 Nakano, K., Matsushima, S., & Kawase, H. (2015). Statistical properties of strong ground motions
862 from the generalized spectral inversion of data observed by K-NET, KiK-net, and the JMA
863 Shindokei network in Japan. *Bull Seismol Soc Am*.**105**, no. 5, 2662-2680.

864 Oth, A., Parolai, S. and Bindi, D., (2011). Spectral analysis of K-NET and KiK-net data in Japan,
865 Part I: Database compilation and peculiarities. Bull Seismol Soc Am. 101, no.2, 652-666.

866 Parolai, S. and Bindi, D., (2004). Influence of soil-layer properties on k evaluation. Bulletin of the
867 Seismological Society of America, 94(1), pp.349-356.

868 Pilz, M. and Cotton, F., 2019. Does the One-Dimensional Assumption Hold for Site Response
869 Analysis? A Study of Seismic Site Responses and Implication for Ground Motion
870 Assessment Using KiK-Net Strong-Motion Data. Earthquake Spectra, 35(2), pp.883-905.

871 Pilz, M., Cotton, F., Zaccarelli, R. and Bindi, D., (2019). Capturing Regional Variations of Hard-
872 Rock Attenuation in Europe. *Bull Seismol Soc Am*.

873 Perron, V., Hollender, F., Bard, P. Y., Gélis, C., Guyonnet-Benaize, C., Hernandez, B., & Ktenidou,
874 O. J. (2017). Robustness of kappa (κ) measurement in low-to-moderate seismicity areas:
875 Insight from a site-specific study in Provence, France. Bull Seismol Soc Am. 107, no.5,
876 2272-2292.

877 Pei, S., Cui, Z., Sun, Y., Toksöz, M.N., Rowe, C.A., Gao, X., Zhao, J., Liu, H., He, J. and Morgan,
878 F.D., 2009. Structure of the upper crust in Japan from S-wave attenuation tomography.
879 Bulletin of the Seismological Society of America, 99(1), pp.428-434.

880 Qin, L., Ben-Zion, Y., Bonilla, L.F. and Steidl, J.H., 2020. Imaging and Monitoring Temporal
881 Changes of Shallow Seismic Velocities at the Garner Valley Near Anza, California,
882 Following the M7. 2 2010 El Mayor-Cucapah Earthquake. Journal of Geophysical
883 Research: Solid Earth, 125(1), p.e2019JB018070.

884 Régnier, J., Cadet, H., Bonilla, L.F., Bertrand, E. and Semblat, J.F., 2013. Assessing nonlinear
885 behavior of soils in seismic site response: Statistical analysis on KiK-net strong-motion
886 data. Bulletin of the Seismological Society of America, 103(3), pp.1750-1770.

887 Régnier, J., Cadet, H. and Bard, P.Y., 2016. Empirical Quantification of the Impact of Nonlinear
888 Soil Behavior on Site ResponseEmpirical Quantification of the Impact of Nonlinear Soil
889 Behavior on Site Response. Bulletin of the Seismological Society of America, 106(4),
890 pp.1710-1719.

Rong, M., Wang, Z., Woolery, E.W., Lyu, Y., Li, X. and Li, S., 2016. Nonlinear site response from the strong ground-motion recordings in western China. Soil Dynamics and Earthquake Engineering, 82, pp.99-110.

Seed, H.B., Wong, R.T., Idriss, I.M. and Tokimatsu, K., 1986. Moduli and damping factors for dynamic analyses of cohesionless soils. *Journal of geotechnical engineering*, 112(11), pp.1016-1032.

Sonnemann, T. and Halldorsson, B., 2017, June. Towards an Automated Kappa Measurement Procedure. In International Conference on Earthquake Engineering and Structural Dynamics (pp. 39-52). Springer, Cham.

Thompson, E.M., Baise, L.G., Tanaka, Y. and Kayen, R.E., 2012. A taxonomy of site response complexity. Soil Dynamics and Earthquake Engineering, 41, pp.32-43.

Trifunac, M.D. and Todorovska, M.I., 1996. Nonlinear soil response—1994 Northridge, California, earthquake. Journal of geotechnical engineering, 122(9), pp.725-735.

Van Houtte, C., Drouet, S., & Cotton, F. (2011). Analysis of the origins of κ (kappa) to compute hard rock to rock adjustment factors for GMPEs. *Bull Seismol Soc Am*.**101**, no. 6, 2926-2941.

Van Houtte, C., Ktenidou, O.J., Larkin, T. and Holden, C., (2014). Hard-site κ 0 (kappa) calculations for Christchurch, New Zealand, and comparison with local ground-motion prediction models. Bull Seismol Soc Am.104, no. 4, 1899-1913.

Xu, B., Rathje, E.M., Hashash, Y., Stewart, J., Campbell, K. and Silva, W.J., 2020. κ 0 for soil sites: Observations from Kik-net sites and their use in constraining small-strain damping profiles for site response analysis. Earthquake Spectra, 36(1), pp.111-137.

913 Yu, G., Anderson, J.G. and Siddharthan, R.A.J., 1993. On the characteristics of nonlinear soil
914 response. Bulletin of the Seismological Society of America, 83(1), pp.218-244.

915 Zalachoris, G. and Rathje, E.M., 2015. Evaluation of one-dimensional site response techniques
916 using borehole arrays. Journal of Geotechnical and Geoenvironmental Engineering,
917 141(12), p.04015053.

Chunyang Ji

Department of Civil, Construction, and Environmental Engineering,

3101 Fitts-Woolard Hall, NC State University

Raleigh, NC 27695, the United States

Email: cji3@ncsu.edu

Ashly Cabas

Department of Civil, Construction, and Environmental Engineering,

3175 Fitts-Woolard Hall, NC State University

Raleigh, NC 27695, the United States

Email: amcabasm@ncsu.edu

Luis Fabian Bonilla

GERS-SRO, Univ. Gustave Eiffel,

F-77447 Marne-la-Vallée, France

Email: luis-fabian.bonilla-hidalgo@univ-eiffel.fr

Céline Gelis

IRSN

Paris Fontenay-aux-Roses, France

Email: celine.gelis@irsn.fr

939 **Table 1.** Local soil conditions, number of ground motions per dataset, predetermined fixed-frequency bandwidth and thresholds for
940 shear strain index, I_γ at all study sites.

Station	V_{s30}[1] (m/s)	V_{s0}[2] (m/s)	$V_{s,depth}$[3] (m/s)	Hole Depth (m)	Number of linear records	Number of transitional records	Number of nonlinear records	1st resonant frequency (Hz)	Predominant frequency (Hz)	f_1[4] (Hz)	f_2[5] (Hz)	$I_{\gamma,0,l}$[6] (%)	$I_{\gamma,0,t}$[7] (%)
AICH17	314	150	2200	101	23	27	12	4.07	4.07	12.65	25.00	0.001	0.003
CHBH13	235	220	2920	1300	139	49	11	1.78	1.78	8.95	25.00	0.001	0.003
FKSH11	240	110	700	115	148	140	26	1.51	9.98	13.97	25.00	0.001	0.003
FKSH14	237	120	1210	147	114	221	28	1.12	4.15	10.05	25.00	0.001	0.007
FKSH18	307	140	2250	100	158	103	16	2.59	5.69	8.95	25.00	0.001	0.003
FKSH19	338	170	3060	100	185	95	21	3.27	3.27	10.05	25.00	0.001	0.003
FKSH21	365	200	1600	200	60	17	8	3.90	3.90	12.65	25.00	0.001	0.003
IBRH16	626	140	2050	300	137	81	15	1.71	7.08	10.05	25.00	0.001	0.003
IBRH17	301	90	2300	510	117	177	18	0.93	9.30	13.01	25.00	0.001	0.007
IBRH20	244	180	1200	923	133	86	11	0.27	0.27	8.95	25.00	0.001	0.007
IWTH21	521	150	2460	100	39	24	6	5.27	5.27	7.38	25.00	0.001	0.003
IWTH26	371	130	680	108	79	32	11	2.12	10.17	14.24	25.00	0.001	0.003
KMMH01	575	150	1900	100	94	24	15	4.03	9.98	13.97	25.00	0.001	0.003
KMMH12	410	210	1000	123	134	34	11	3.27	8.17	11.44	25.00	0.001	0.003
MYGH07	366	130	740	142	59	39	11	0.93	8.61	12.06	25.00	0.001	0.003
MYGH10	348	110	770	205	229	132	16	0.95	10.66	14.93	25.00	0.001	0.007
NGNH29	465	150	1040	110	81	38	16	1.95	6.93	10.05	25.00	0.001	0.003
NIGH07	528	200	1600	106	29	10	11	4.12	7.08	10.05	25.00	0.001	0.003
NIGH12	553	240	780	110	29	9	11	2.00	5.00	12.65	25.00	0.001	0.003
TCGH16	213	80	680	112	112	334	35	1.27	4.81	11.27	25.00	0.001	0.007

941 [1] V_{s30}: time averaged shear-wave velocity in the top 30 m of the soil profile

942 [2] V_{s0}: shear-wave at the ground surface

943 [3] $V_{s,depth}$: shear-wave velocity at the depth of the borehole sensor

944 [4]f_1: the lower frequency limit to estimate individual κ_r

945 [5]f_2: the upper frequency limit to estimate individual κ_r

946 [6]$I_{\gamma,0,l}$: the shear-strain index threshold to separate linear and transitional datasets

947 [7]$I_{\gamma,0,t}$: the shear-strain index threshold to separate transitional and nonlinear datasets

948

949 **Table 2.** Ground motion datasets constructed via alternative approaches (AP1 to AP4) explored
950 in this study to implement the κ_0-model.

Approach	$\kappa_{0\_lin\_sur}$	$\kappa_{0\_nl\_sur}$	$\kappa_{0\_tran\_sur}$	κ_{0_depth}	κ_0-model
AP1	Linear dataset	Nonlinear dataset	--	Borehole dataset	Equation (5)
AP2	Linear and transitional datasets	Nonlinear dataset	--	Borehole dataset	Equation (5)
AP3	Linear dataset	Nonlinear and transitional datasets	--	Borehole dataset	Equation (5)
AP4	Linear dataset	Nonlinear dataset	Transitional datasets	Borehole dataset	Equation (5)

951

952 **Table 3.** Site-specific κ_0 values obtained from different dataset definitions at stations FKSH14
953 and MYGH10.

	Approach	$\kappa_{0\_lin\_sur}$ (s)	$\kappa_{0\_nl\_sur}$ (s)	$\kappa_{0\_tran\_sur}$ (s)
FKSH14	AP1	0.0488	0.0633	--
	AP2	0.0565	0.0638	--
	AP3	0.0500	0.0607	--
	AP4	0.0499	0.0638	0.0602
	Maximum difference	15.83%	5.10%	
MYGH10	AP1	0.0567	0.0563	--
	AP2	0.0568	0.0560	--
	AP3	0.0559	0.0572	--
	AP4	0.0560	0.0558	0.0575
	Maximum difference	1.56%	2.53%	

954

955

956

957

958

959 **Table 4.** T-test results for κ_{0_pred} values estimated with linear and nonlinear datasets defined by

960 AP3 (which includes records categorized as transitional into the nonlinear dataset).

Station	V_{s30} (m/s)	p-value	Statistically different
		Linear κ_{0_pred} vs. nonlinear κ_{0_pred}*	
AICH17	314	10.37%	--
CHBH13	235	<0.01%	Yes
FKSH11	240	1.07%	Yes
FKSH14	237	<0.01%	Yes
FKSH18	307	2.36%	Yes
FKSH19	338	57.66%	--
FKSH21	365	47.12%	--
IBRH16	626	13.80%	--
IBRH17	301	55.92%	--
IBRH20	244	5.97%	--
IWTH21	521	9.23%	--
IWTH26	371	0.62%	Yes
KMMH01	575	0.32%	Yes
KMMH12	410	3.38%	Yes
MYGH07	366	0.04%	Yes
MYGH10	348	7.45%	--
NGNH29	465	72.74%	--
NIGH07	528	88.97%	--
NIGH12	553	66.61%	--
TCGH16	213	<0.01%	Yes

961

962 *The transitional dataset is included into the nonlinear dataset (i.e., datasets following the criteria of AP3).

963 **List of Figure Captions:**

964 **Figure 1.** Comparisons between a weak and a strong ground motion recorded at FKSH14 (V_{s30} =
965 237 m/s). The M_w and R_e are 4 and 15 km for the low-intensity ground motion, while 5.1 and 15
966 km for the high-intensity ground motion. The frequency window ([10.05, 30] Hz) applied in this
967 plot is picked manually. The left and right columns correspond to analyses conducted on the
968 horizontal components H_1 and H_2, respectively. The color version of this figure is available only
969 in the electronic version of this article.

970 **Figure 2.** (a) Locations of selected Japanese recording stations in this study, and (b) magnitude
971 and distance distribution of selected ground motions.

972 **Figure 3.** Hyperbolic models fitted to observed PGA_{rotD50} and $I_{\gamma,0}$ data at four study sites. The V_{s30}
973 for IBRH16, IBRH17, IBRH20, and IWTH21 are 626, 301, 244, and 521 m/s, respectively.

974 **Figure 4**. Surface PGA_{rotD50} against $I_{\gamma,0}$ at MYGH10 (V_{s30} = 348 m/s). The red dot-dashed lines
975 present the linear ($I_{\gamma,0,l}$) and transitional ($I_{\gamma,0,t}$) thresholds for $I_{\gamma,0}$. The color version of this figure is
976 available only in the electronic version of this article.

977 **Figure 5.** G/G_{max} versus $I_{\gamma,0}$ at study sites. The G_{max} is computed from the average values of
978 $\left(\frac{PGA_{rotD50}}{PGV_{rotD50}/V_{s,0}}\right)$ for records with $I_{\gamma,0}$ less than 0.001%. The colors represent PGA_{rotD50} values. The
979 color version of this figure is only available in the electronic version of this article. The color
980 version of this figure is available only in the electronic version of this article.

981 **Figure 6.** Comparisons of individual κ_r estimates from our automated algorithm, $\kappa_{r,auto}$, and the
982 fixed-frequency band method, κ_{r_AS} at FKSH14 (V_{s30} = 237 m/s) for surface (left) and borehole
983 (right) records. The color version of this figure is available only in the electronic version of this
984 article.

985 **Figure 7**. Surface κ_{r_AS} estimates and their corresponding PGA_{rotD50}, $I_{\gamma,0}$ and R_e values for selected
986 ground motions recorded at (a) FKSH14 (V_{s30} = 237 m/s) and (b) MYGH10 (V_{s30} = 348 m/s).
987 Different colors represent varying epicentral distances per record, and the size of markers indicate
988 the corresponding PGA_{rotD50}. The color version of this figure is only available in the electronic
989 version of this article. The color version of this figure is available only in the electronic version of
990 this article.
991 **Figure 8**. κ_0-model at FKSH14 (V_{s30} = 237 m/s) from datasets defined by (a) AP1, which only
992 considers the linear and nonlinear datasets, (b) AP2, where transitional records are included as part
993 of the linear dataset, (c) AP3, where transitional records are included as part of the nonlinear
994 dataset, and (d) AP4, where the linear, transitional, and nonlinear datasets are considered
995 separately. The color version of this figure is available only in the electronic version of this article.
996 **Figure 9**. κ_0-model at MYGH10 (V_{s30} = 348 m/s) with datasets defined by (a) AP1, which only
997 considers the linear and nonlinear datasets, (b) AP2, where transitional records are included as part
998 of the linear dataset, (c) AP3, where transitional records are included as part of the nonlinear
999 dataset, and (d) AP4, where the linear, transitional, and nonlinear datasets are considered
1000 separately. The color version of this figure is only available in the electronic version of this article.
1001 The color version of this figure is available only in the electronic version of this article.
1002 **Figure 10.** Ratio of $\kappa_{0\_nl\_sur}/\kappa_{0\_lin\_sur}$ at study sites estimated using the dataset definitions based on
1003 AP3 (left panel) and AP4 (right panel) against to V_{s5}, V_{s10}, and V_{s30}. The color version of this
1004 figure is available only in the electronic version of this article.
1005 **Figure 11.** Estimated surface κ_{0_pred} and their corresponding ground shaking intensity and in situ
1006 deformation characterized by PGA_{rotD50} and $I_{\gamma,0}$, respectively at (a) FKSH14 (V_{s30} = 237 m/s) and
1007 (b) MYGH10 (V_{s30} = 348 m/s). Both, the color and the size of markers represent varying PGA_{rotD50}

values. Triangles and circles represent the linear and nonlinear datasets defined by AP3. The red dashed lines depict the local regression model based on the κ_{0_pred} and $I_{\gamma,0}$ data. The color version of this figure is only available in the electronic version of this article. The color version of this figure is available only in the electronic version of this article.

Figure 12. Observed distribution of κ_{0_pred} at (a) FKSH14 (V_{s30} = 237 m/s) and (b) MYGH10 (V_{s30} = 348 m/s) for the linear and nonlinear datasets. The red lines depict the theoretical probability density function (PDF) fitted with a Gaussian distribution. The color version of this figure is available only in the electronic version of this article.

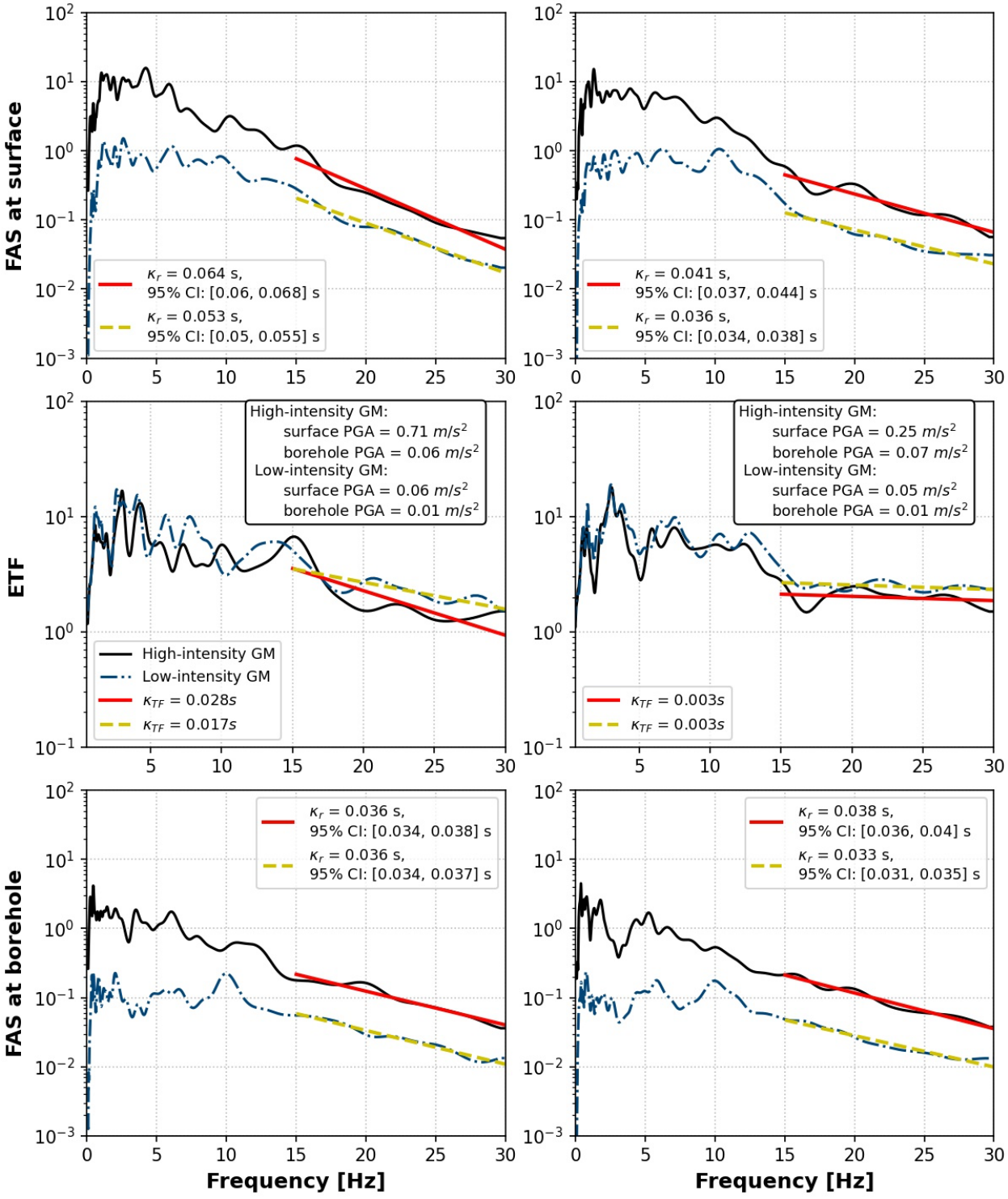

Figure 1. Comparisons between a weak and a strong ground motion recorded at FKSH14 (V_{s30} = 237 m/s). The M_w and R_e are 4 and 15 km for the low-intensity ground motion,

1021 while 5.1 and 15 km for the high-intensity ground motion. The frequency window ([10.05,
1022 30] Hz) applied in this plot is picked manually. The left and right columns correspond to
1023 analyses conducted on the horizontal components H_1 and H_2, respectively. The color
1024 version of this figure is available only in the electronic version of this article.

1025

1026

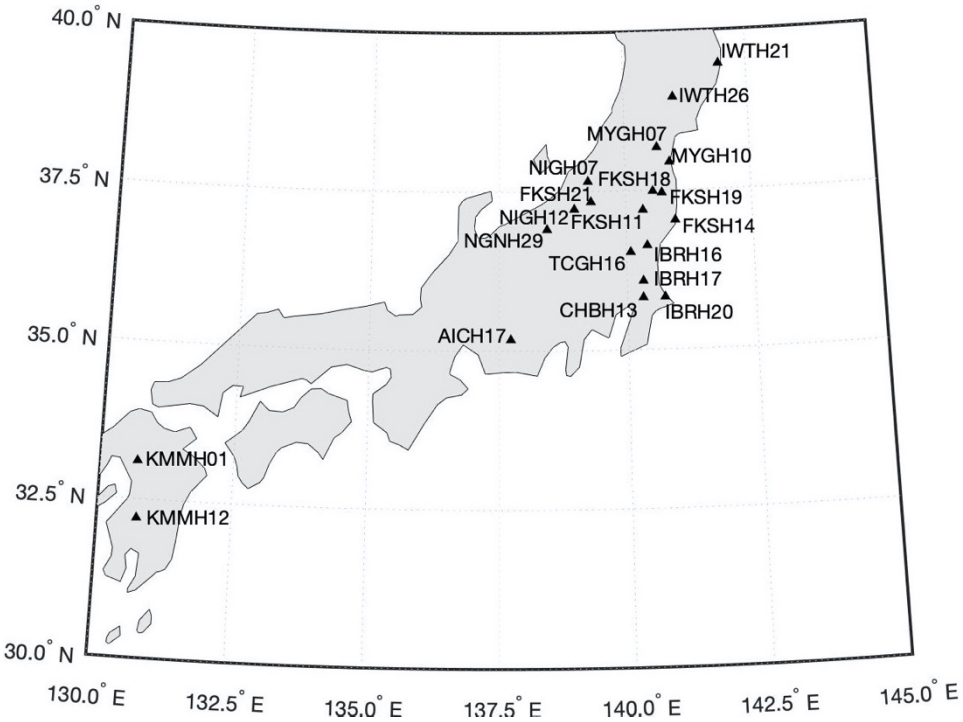

1027

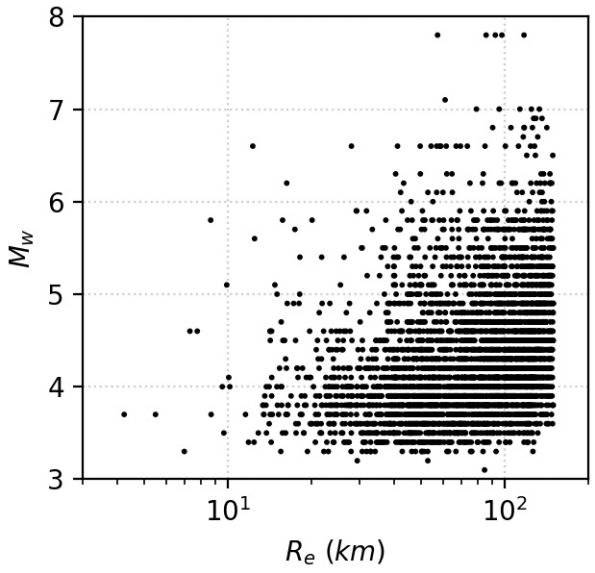

1028

1029 **Figure 2.** (a) Locations of selected Japanese recording stations in this study, and (b) magnitude

1030 and distance distribution of selected ground motions.

1031

1032

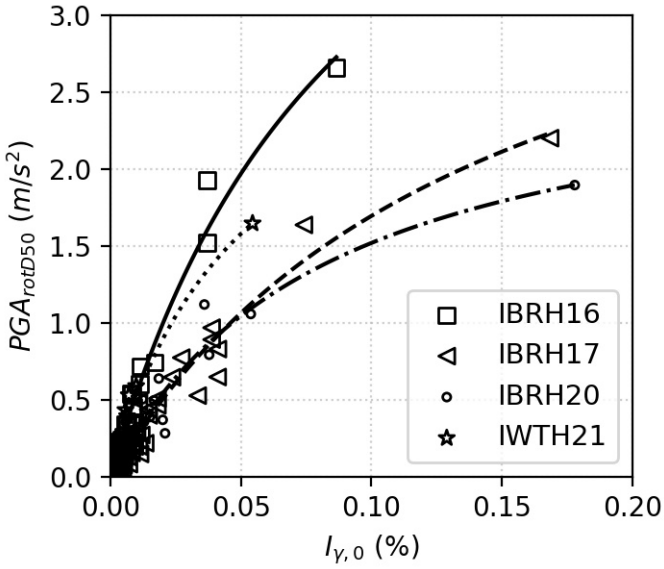

1033

1034 **Figure 3.** Hyperbolic models fitted to observed PGA_{rotD50} and $I_{\gamma,0}$ data at four study sites. The

1035 V_{s30} for IBRH16, IBRH17, IBRH20, and IWTH21 are 626, 301, 244, and 521 m/s, respectively.

1036

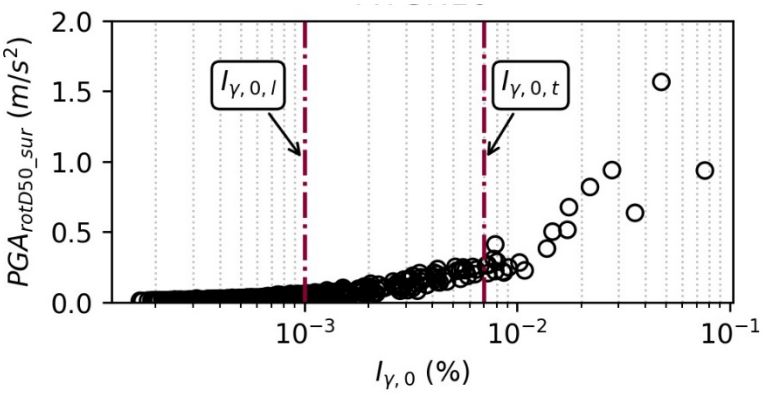

1037

1038 **Figure 4**. Surface PGA_{rotD50} against $I_{\gamma,0}$ at MYGH10 (V_{s30} = 348 m/s). The red dot-dashed lines

1039 present the linear ($I_{\gamma,0,l}$) and transitional ($I_{\gamma,0,t}$) thresholds for $I_{\gamma,0}$. The color version of this figure

1040 is available only in the electronic version of this article.

1041

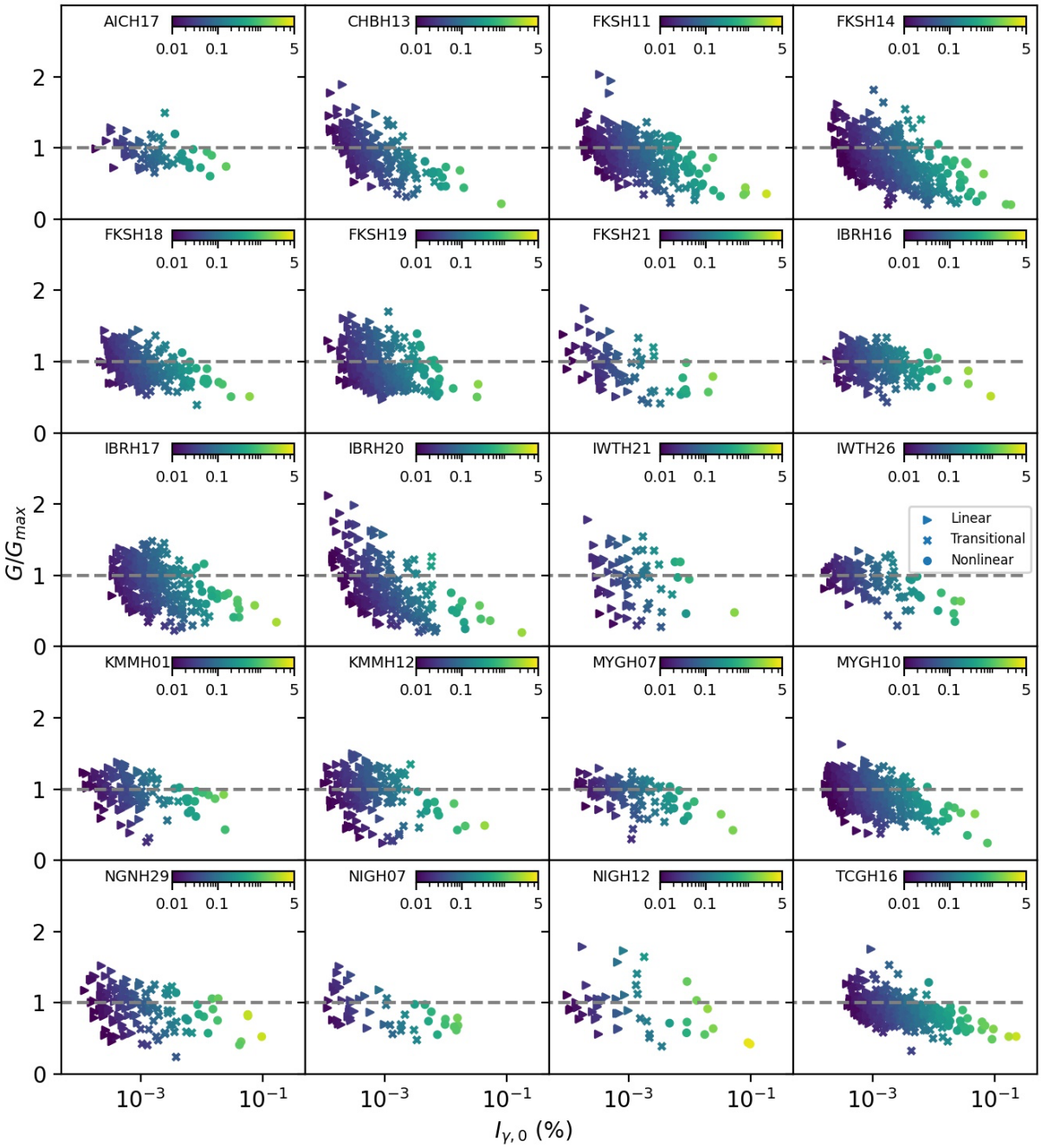

Figure 5. G/G_{max} versus $I_{\gamma,0}$ at study sites. The G_{max} is computed from the average values of $\left(\frac{PGA_{rotD50}}{PGV_{rotD50}/V_{s,0}}\right)$ for records with $I_{\gamma,0}$ less than 0.001%. The colors represent PGA_{rotD50} values (in units of m/s^2). The color version of this figure is only available in the electronic version of this article. The color version of this figure is available only in the electronic version of this article.

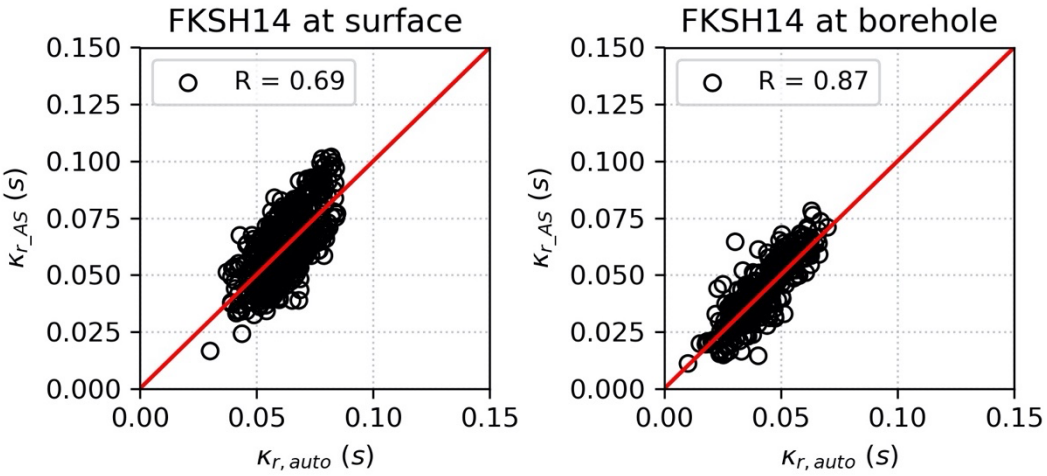

Figure 6. Comparisons of individual κ_r estimates from our automated algorithm, $\kappa_{r,auto}$, and the fixed frequency band method, κ_{r_AS} at FKSH14 (V_{s30} = 237 m/s) for surface (left) and borehole (right) records. The color version of this figure is available only in the electronic version of this article.

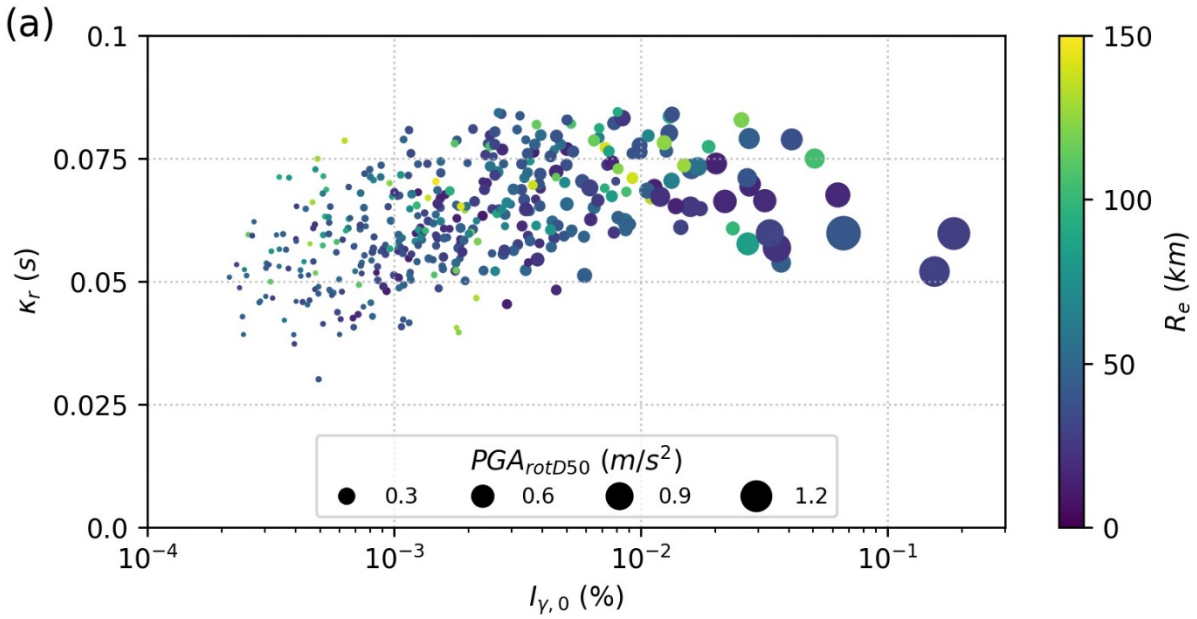

1054

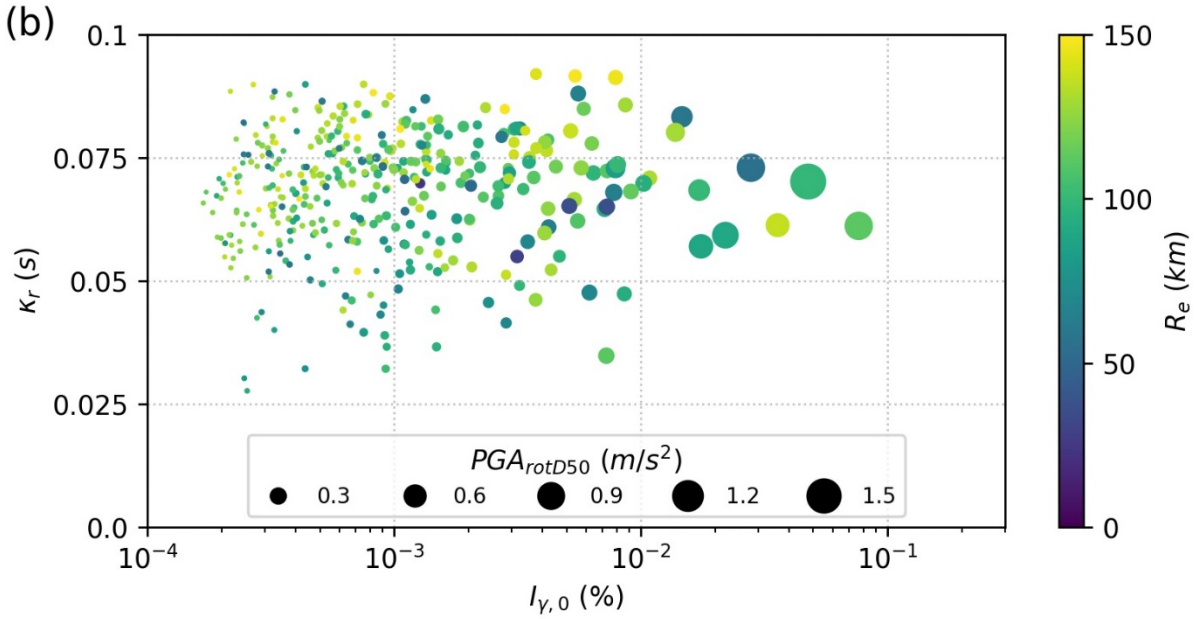

1055

1056 **Figure 7**. Surface κ_{r_AS} estimates and their corresponding PGA_{rotD50}, $I_{\gamma,0}$ and R_e values for
1057 selected ground motions recorded at (a) FKSH14 (V_{s30} = 237 m/s) and (b) MYGH10 (V_{s30} = 348
1058 m/s). Different colors represent varying epicentral distances per record, and the size of markers
1059 indicate the corresponding PGA_{rotD50}. The color version of this figure is only available in the
1060 electronic version of this article. The color version of this figure is available only in the
1061 electronic version of this article.
1062

1063

1064

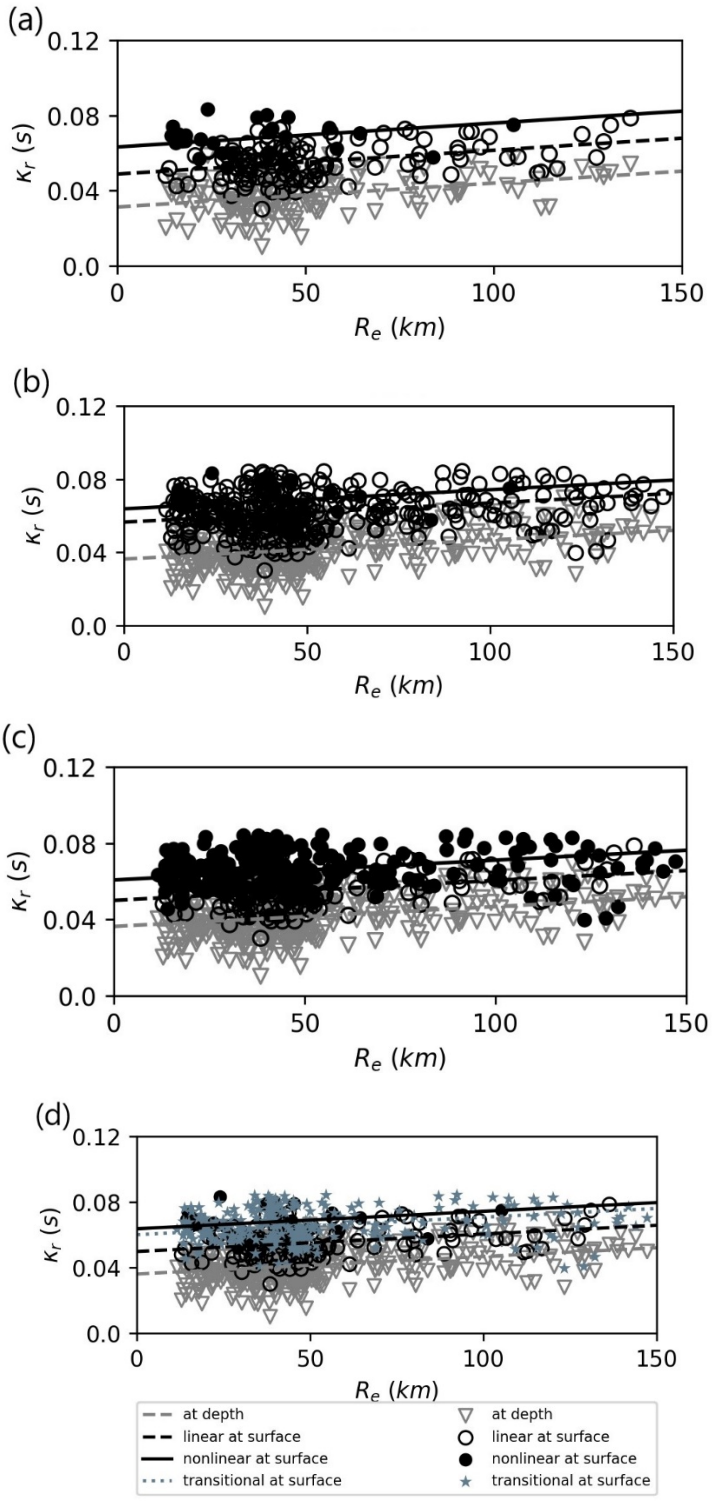

1065

1066

1067

1068

Figure 8. κ_0-model at FKSH14 (V_{s30} = 237 m/s) from datasets defined by (a) AP1, which only considers the linear and nonlinear datasets, (b) AP2, where transitional records are included as part of the linear dataset, (c) AP3, where transitional records are included as part of the nonlinear dataset, and (d) AP4, where the linear, transitional, and nonlinear datasets are considered separately. The color version of this figure is only available in the electronic version of this article.

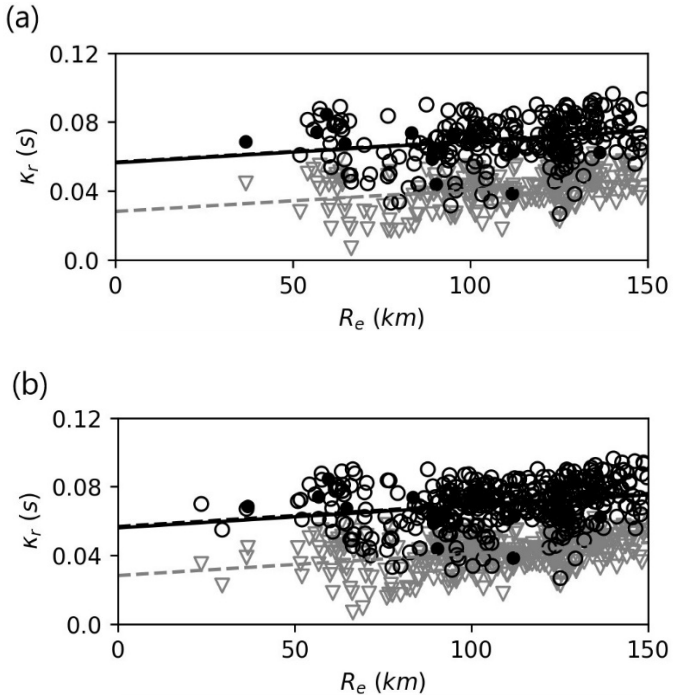

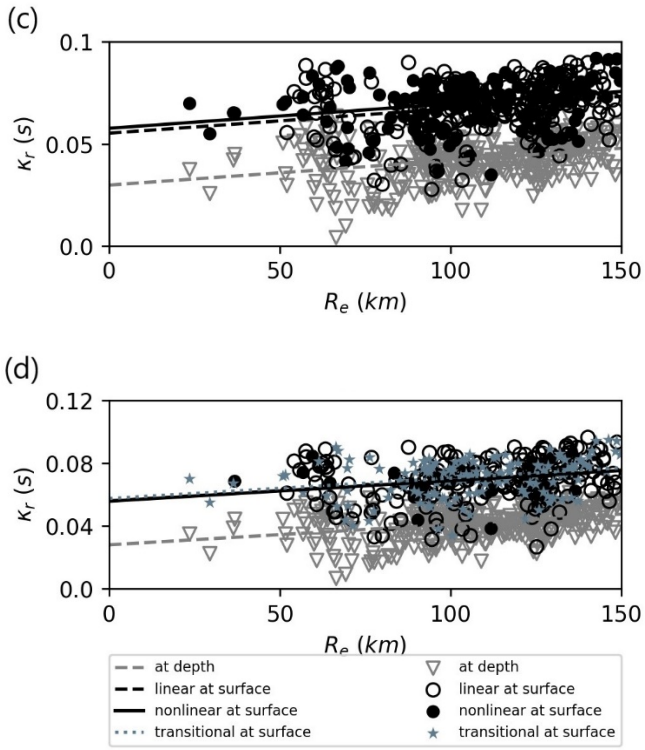

Figure 9. κ_0-model at MYGH10 (V_{s30} = 348 m/s) with datasets defined by: (a) AP1, which only considers the linear and nonlinear datasets, (b) AP2, where transitional records are included as part of the linear dataset, (c) AP3, where transitional records are included as part of the nonlinear dataset, and (d) AP4, where the linear, transitional, and nonlinear datasets are considered separately. The color version of this figure is available only in the electronic version of this article.

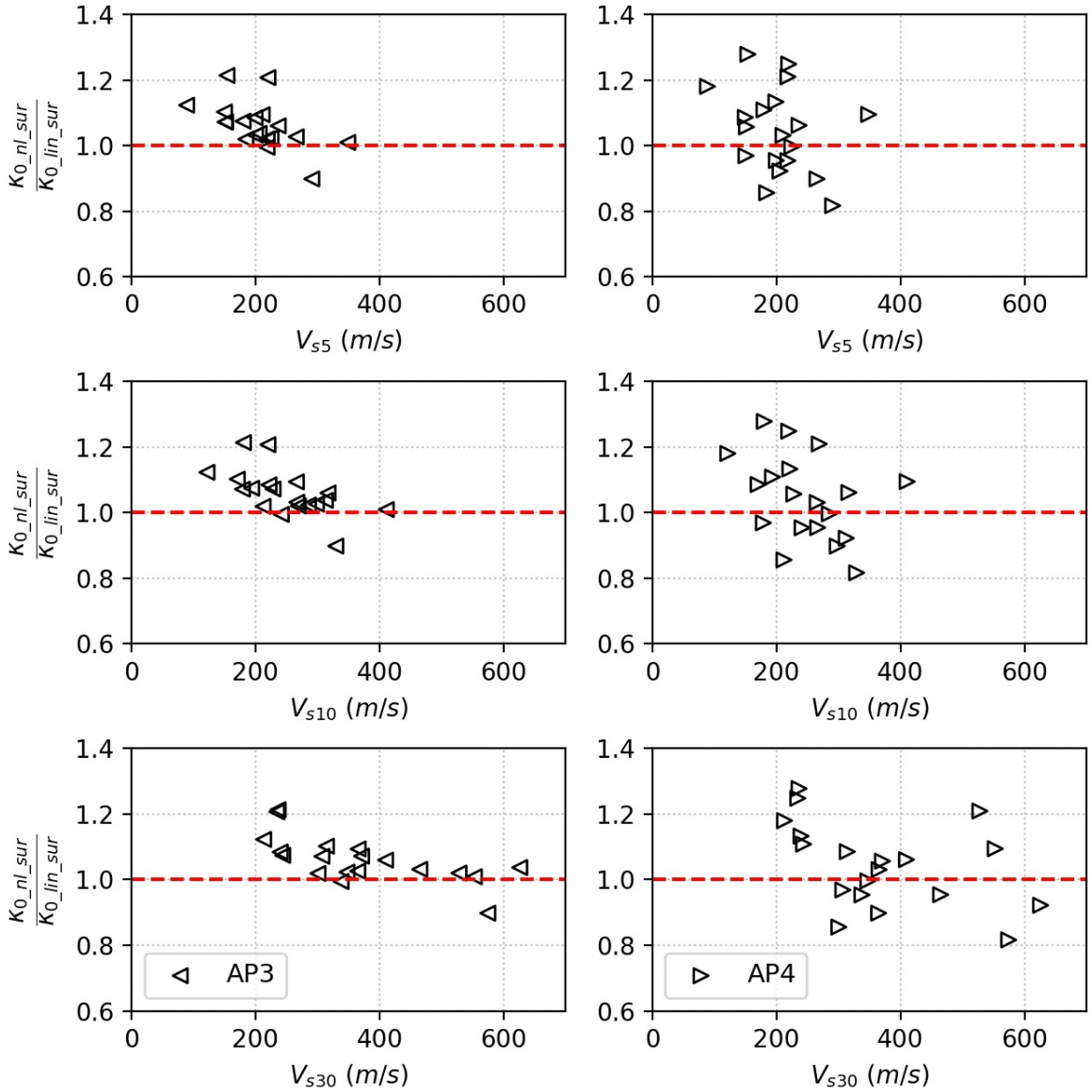

Figure 10 Ratio of $\kappa_{0\_nl\_sur}/\kappa_{0\_lin\_sur}$ at study sites estimated using the dataset definitions based on AP3 (left panel) and AP4 (right panel) against to V_{s5}, V_{s10}, and V_{s30}. The color version of this figure is available only in the electronic version of this article.

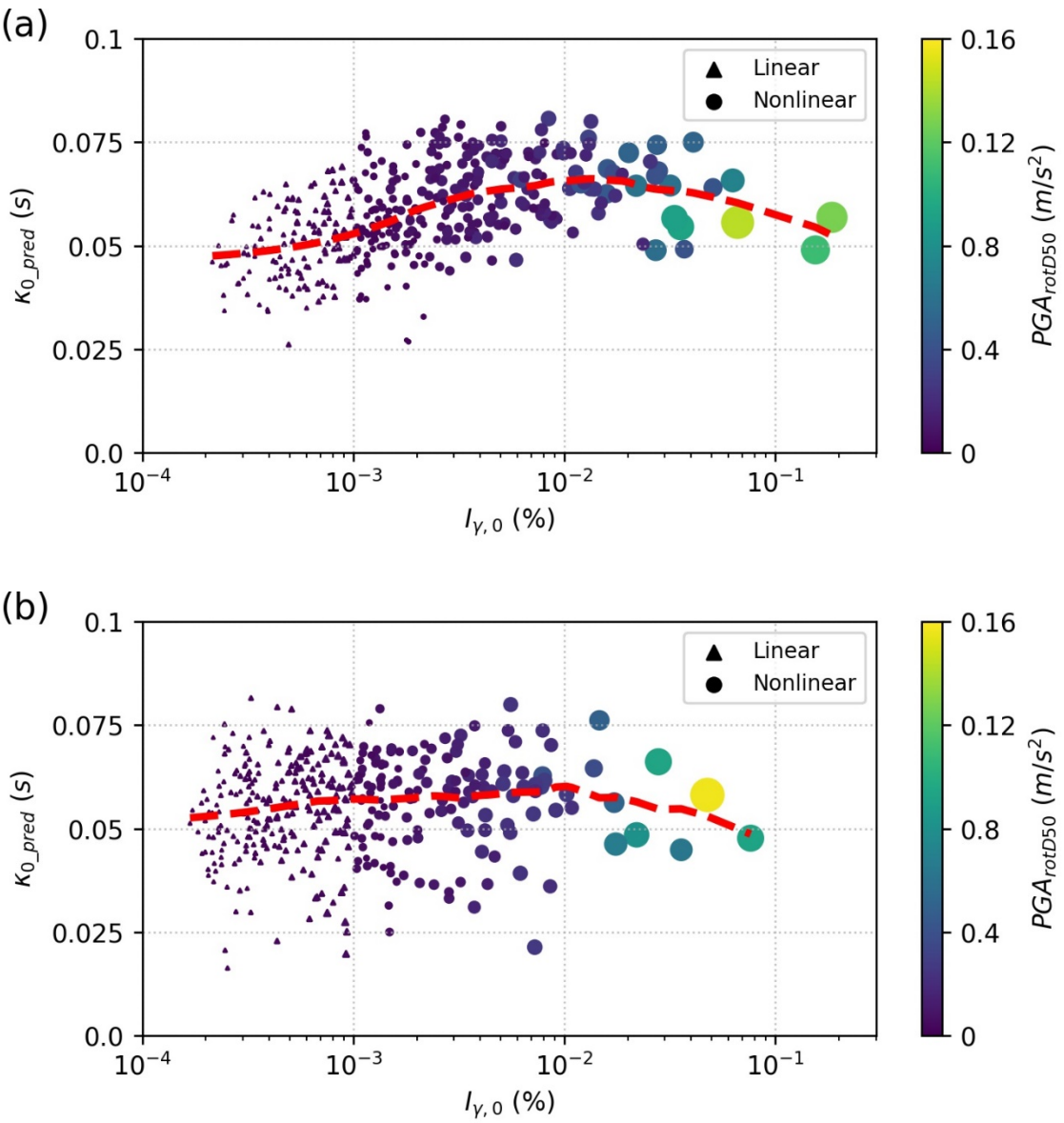

Figure 11. Estimated surface κ_{0_pred} and their corresponding ground shaking intensity and in situ deformation characterized by PGA_{rotD50} and $I_{\gamma,0}$, respectively at (a) FKSH14 (V_{s30} = 237 m/s) and (b) MYGH10 (V_{s30} = 348 m/s). Both, the color and the size of markers represent varying PGA_{rotD50} values. Triangles and circles represent the linear and nonlinear datasets defined by AP3. The red dashed lines depict the local regression model based on the κ_{0_pred} and $I_{\gamma,0}$ data. The color version of this figure is only available in the electronic version of this article. The color version of this figure is available only in the electronic version of this article.

1104

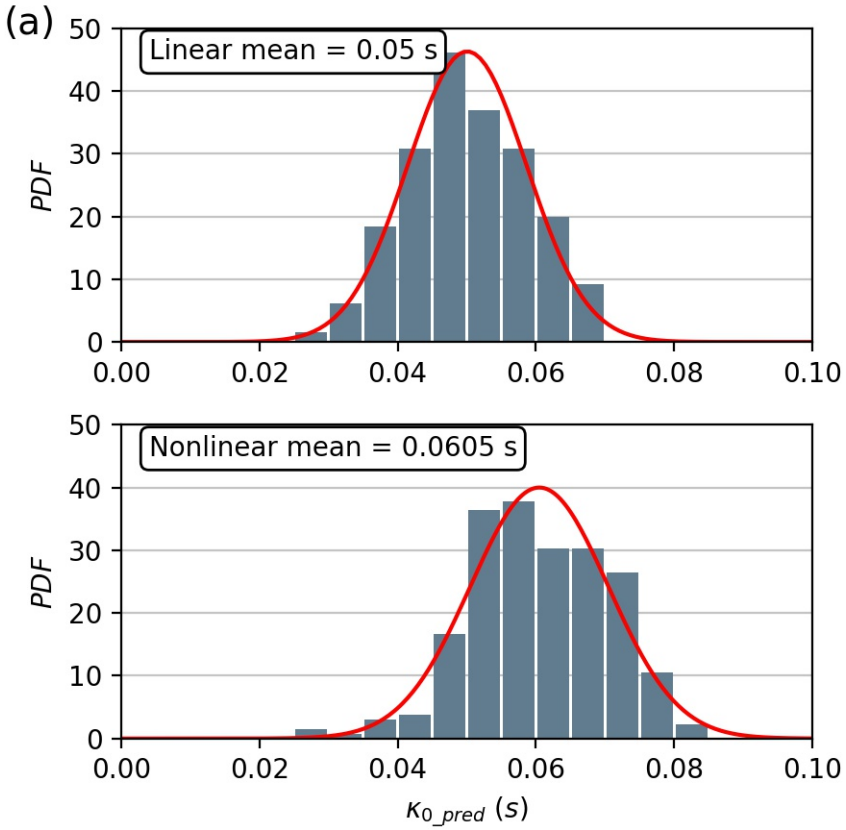
(a)
Linear mean = 0.05 s
Nonlinear mean = 0.0605 s
PDF
PDF
0
10
20
30
40
50
0.00
0.02
0.04
0.06
0.08
0.10
κ_{0_pred} (s)

1105

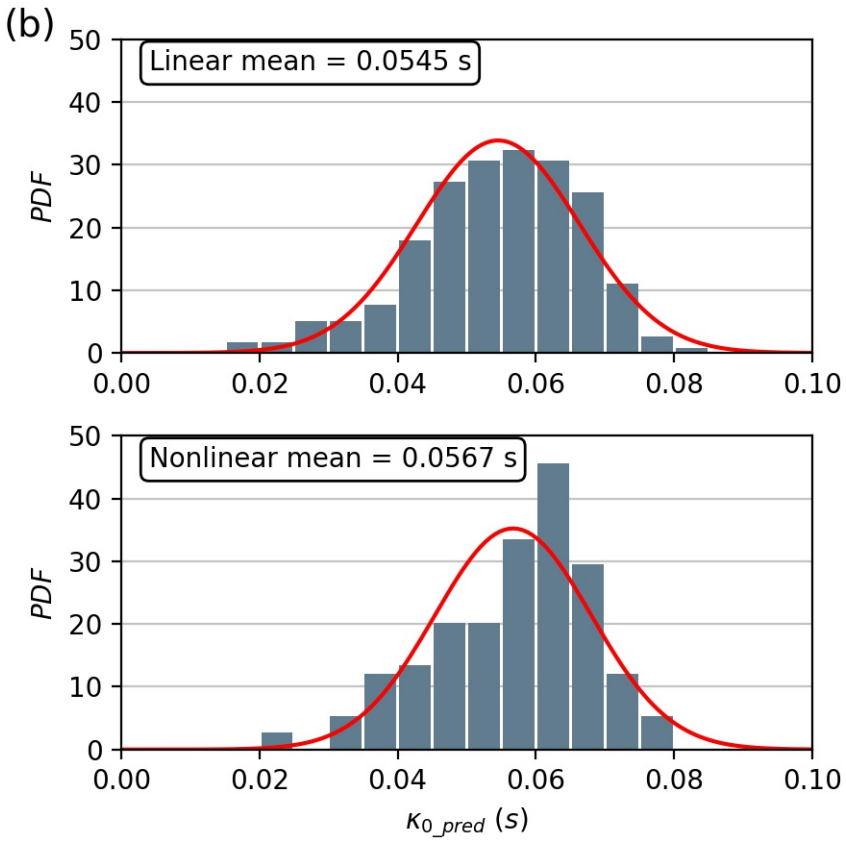

Figure 12. Observed distribution of κ_{0_pred} at (a) FKSH14 (V_{s30} = 237 m/s) and (b) MYGH10 (V_{s30} = 348 m/s) for the linear and nonlinear datasets. The red lines depict the theoretical probability density function (PDF) fitted with a Gaussian distribution. The color version of this figure is available only in the electronic version of this article.